JGR Atmospheres

RESEARCH ARTICLE
10.1029/2023JD039319

The Development of Atmospheric Bores in Non-Uniform Baroclinic Environments and Their Roles in the Maintenance, Structure, and Evolution of an MCS

Shushi Zhang[1,2,3], David B. Parsons[4], Xin Xu[5,6], Hong Huang[7], Fen Xu[1], Tianjie Wu[1], Gang Chen[1], Abuduwaili Abulikemu[8], Yating Zhao[5], Shengxi Zhang[9], and Ying Tang[10]

[1]Key Laboratory of Transportation Meteorology of China Meteorological Administration, Nanjing Joint Institute for Atmospheric Sciences, Nanjing, China, [2]State Key Laboratory of Severe Weather, Chinese Academy of Meteorological Sciences, Beijing, China, [3]High Impact Weather Key Laboratory of CMA, Changsha, China, [4]School of Meteorology, University of Oklahoma, Norman, OK, USA, [5]Key Laboratory of Mesoscale Severe Weather/MOE and School of Atmosphere Sciences, Nanjing University, Nanjing, China, [6]State Key Laboratory of Severe Weather and Joint Center for Atmospheric Radar Research of CMA/NJU, Beijing, China, [7]College of Meteorology and Oceanography, National University of Defense Technology, Changsha, China, [8]Key Laboratory of Oasis Ecology (Ministry of Education), College of Resources and Environment Sciences, Xinjiang University, Urumqi, China, [9]Yixing Meteorological Bureau, Yixing, China, [10]Nanjing Marine Radar Institute, Nanjing, China

Key Points:

- Atmospheric bores are generated within a nocturnal mesoscale convective system in a non-uniform environment
- The mesoscale variations in the environment ahead of the mesoscale convective system (MCS) modify the structure of the bores, which impact the organization of the MCS
- The intrusion of the convective downdraft into the nocturnal boundary layer plays a critical role in generating bores over the southern North China Plain

Correspondence to:
X. Xu,
xinxu@nju.edu.cn

Citation:
Zhang, S., Parsons, D. B., Xu, X., Huang, H., Xu, F., Wu, T., et al. (2024). The development of atmospheric bores in non-uniform baroclinic environments and their roles in the maintenance, structure, and evolution of an MCS. *Journal of Geophysical Research: Atmospheres*, *129*, e2023JD039319. https://doi.org/10.1029/2023JD039319

Received 26 MAY 2023
Accepted 20 DEC 2023

Author Contributions:
Conceptualization: Shushi Zhang, David B. Parsons
Data curation: Shushi Zhang, Fen Xu, Gang Chen
Formal analysis: Shushi Zhang
Funding acquisition: David B. Parsons, Xin Xu, Hong Huang, Fen Xu, Shengxi Zhang
Investigation: Shushi Zhang
Methodology: Shushi Zhang, David B. Parsons
Project Administration: Hong Huang
Resources: Shushi Zhang, Yating Zhao
Software: Tianjie Wu, Abuduwaili Abulikemu, Ying Tang
Supervision: David B. Parsons, Xin Xu
Visualization: Shushi Zhang
Writing – original draft: Shushi Zhang
Writing – review & editing: David B. Parsons, Xin Xu

Abstract This study used radar observations and a high-resolution numerical simulation to explore the interactions between an mesoscale convective system (MCS), cold pool outflows, and atmospheric bores in a non-uniform baroclinic environment. The bores were generated by a nocturnal MCS that occurred on 2–3 June 2017 over the southern North China Plain. The goal of this investigation is to determine how the structure of bores varied within this non-uniform environment and whether and how the bores would maintain the MCS and alter its structure. To the southwest of the MCS, where there was large CAPE and a well-mixed boundary layer, discrete convection initiation occurred behind a single radar fine line (RFL) maintaining the propagation of the MCS. To the southeast of the MCS, multiple RFLs were found suggesting the generation of an undular bore in an environment containing an intense nocturnal stable boundary layer with dry upper layers and little CAPE. Hydraulic and nonlinear theory were applied to the simulation of the MCS revealing that the differences in the bore evolution depended on both the characteristics of the cold pool and the variations in the ambient environment. Thus, the characteristics of the ambient environment and the associated differences in bore structure impacted the maintenance and organization of the MCS. This study implies the importance of an accurate representation of the low-level ambient environment and the microphysics and kinematics within the MCS to accurately simulate and forecast cold pools, the generation and evolution of bores, and their impact on nocturnal MCSs.

Plain Language Summary Convective storms that occur during the day are often maintained by the lifting of low-level air by storm outflows. At night when a low-level stable layer forms, these outflows can generate an atmospheric bore, which is a type of gravity wave response. Investigations at numerous locations worldwide have demonstrated that bores contribute to the initiation and maintenance of nocturnal convective systems. However, relatively few studies have concentrated on how a non-uniform nocturnal environment can change the structure of bores and their impact on convection. This study examines how bores and convection interact over the southern North China Plain (SNCP) where the nocturnal environment during warm season is often non-uniform. These environmental variations impacted the generation and evolution of the bores altering the storm structure. The bores over the SNCP also had a unique generation mechanism forming when a strong downdraft penetrated into a moist layer. This study shows that an accurate representation of both the ambient environment and the storm microphysics and kinematics are likely necessary to improve the forecast accuracy of the nocturnal convective systems, particularly over regions with a non-uniform environment, such as the SNCP.

1. Introduction

Nocturnal Mesoscale Convective Systems (MCSs) are the key factor causing the nighttime maximum in warm season precipitation over land masses in numerous regions (e.g., Carbone et al., 2002; Laing & Fritsch, 1993 and references therein). Nocturnal MCSs have long been recognized to cause flash flooding (e.g., Maddox et al., 1980)

with more recent studies (e.g., Houze, 2018 and references therein) demonstrating a clear linkage between nocturnal convection and high-impact weather. Unfortunately, an accurate representation of nocturnal MCSs remains a critical challenge in weather and climate modeling (Bechtold et al., 2014; Becker et al., 2021; Clark, 2017; Fritsch & Carbone, 2004; Geerts et al., 2017; Peters et al., 2017; Tang et al., 2021). These challenges arise as a result of the simulation's sensitivity to the initial conditions, model physics, resolution (Duda et al., 2014; Morrison et al., 2009; Stensrud et al., 2000), the ambient environment (Corfidi et al., 2008; Reif & Bluestein, 2017) and the self-organizing nature of MCSs especially as MCSs evolve during the night (Parker, 2021).

As part of the self-organizing nature of MCSs, convectively generated cold pools can help maintain convection through lifting of the boundary layer air in the ambient environment. At night, the cold pool ascent can potentially fail to directly maintain deep convection due to the presence of a nocturnal stable boundary layer (NSL). However, cold pools in this nocturnal environment can also generate bores which often result in little change in the surface temperature but cause lifting of the lower tropospheric air by up to ∼1 km (e.g., Loveless et al., 2019; Parsons et al., 2019). This ascent associated with bores establishes a favorable environment for the initiation and/or maintenance of nocturnal convection. An atmospheric bore is a gravity wave response that occurs when a convectively generated density current intrudes on a low-level stable layer (Rottman & Simpson, 1989). Bores often form as non-undular or undular disturbances (e.g., Haghi et al., 2017). Bores can often be visualized on radar as having the appearance of a ripple or ripples created when a frog swims near the surface of a shallow pond.

Bores have been observed and examined over Australia (Birch & Reeder, 2013; Davies et al., 2017; Watson & Lane, 2016), the UK (Osborne & Lapworth, 2017), Mexico (Martin & Johnson, 2008), South America (Lombardo & Kumjian, 2022), and China (Zhang et al., 2022). Numerous studies have investigated bores generated by nocturnal MCSs over the Southern Great Plains (SGP) of the United States (e.g., Blake et al., 2017; Chasteen et al., 2019; Haghi et al., 2017; Knupp, 2006; Koch, Feltz, et al., 2008; Koch, Flamant, et al., 2008 and references therein). These nocturnal MCSs often originate over the Rocky Mountains and/or on the higher elevation of the Great Plains to the west due to afternoon heating (Cotton et al., 1983; Wetzel et al., 1983). Subsequently, organized MCS form and move eastward across the Great Plains (e.g., Carbone & Tuttle, 2008; Keenan & Carbone, 2008; Parker & Ahijevych, 2007). This eastward-moving envelope of deep convection passes over the SGP throughout the night. Bores tend to form when convectively generated density currents encounter the NSL. Bores can persist for hours and are usually maintained by a wave ducting mechanism provided by the nocturnal, southerly low-level jet over the SGP (e.g., Haghi & Durran, 2021; Haghi et al., 2019).

The deep lifting of the lower tropospheric environmental flow by bores can help maintain an MCS through reducing the convective inhibition (CIN) of the environment and/or initiating new convective cells (e.g., French & Parker, 2010; Loveless et al., 2019; Parsons et al., 2019). However, the interaction between bores and the nocturnal environment is more complicated than the well-known conceptual paradigm of cold pool ascent that leads to a squall line with a trailing stratiform MCSs. For example, the ascent produced by the bore can create a favorable environment for nocturnal convection by lifting the ambient environment sufficiently so that the trailing cold pool triggers new convection (Koch & Clark, 1999). Bores can also lead to discrete propagation of an MCS by triggering new convective cells well ahead of the MCS's cold pool (Blake et al., 2017; Zhang, Parsons, & Wang, 2020). In addition to playing a role in initiating new convective cells within an MCS, the lifting by bores leaves an air mass more conducive to deep convection that can cover an area of up to 10,000 km^2 and last for many hours (Parsons et al., 2019).

A well-known nocturnal maximum in rainfall occurs over the Central and North Plains of China region (Guan et al., 2020; Yu et al., 2007) associated with a secondary peak in the frequency of MCSs during the early morning hours (Yang et al., 2015). While bores have been shown to often be associated with nocturnal convection, bores in China have received little attention until the recent Zhang, Parsons, Xu, et al. (2020) study of an atmospheric bore generated by a nocturnal MCS over the southern North China Plain (SNCP). Given the eastward-moving envelopes of nocturnal convection over the SNCP that initially formed over the sloped, elevated terrain to the west, favorable conditions for bore generation exist over the SNCP and even the entire North China Plain (NCP). However, the diverse flow regimes that exist over the SNCP during the warm season leads to a complicated situation for the generation, evolution, and maintenance of bores and their impacts on the MCSs (Zhang et al., 2022). This complicated situation includes, for example, convection generating weak cold pools (Liu & Moncrieff, 2017) in an environment of relatively low vertical wind shear (Meng & Zhang, 2012).

The evolution of the bore-cold pool interaction is also more complicated over the SNCP as Zhang, Parsons, Xu, et al. (2020) found that the leading edge of a weak cold pool can separate from the main cold pool (i.e., feeder flow), propagating away from the MCS, and subsequently take on the structure of an undular bore. This evolution, while expected from theory (e.g., Rottman & Simpson, 1989), has not been observed and well documented to occur over other regions. In addition, during the spring the region over central and east China is characterized by the presence of the Mei-yu front, a warm-season quasi-stationary, east–west-oriented frontal zone. The Mei-yu front is characterized by a weak temperature gradient but with a strong contrast in moisture across the frontal boundary with spatial variations in the nocturnal low-level jet (NLLJ) (Guan et al., 2020). These variations will impact the structure and evolution of bores. For example, bores associated with MCSs occurring along the Mei-yu front often propagate from southwest (SW) to northeast (NE) in contrast to the general southward propagation of bores over the SGP (Zhang et al., 2022).

Understanding the evolution of the cold pool-bore interactions in this complex spatially varying environment requires going beyond previous studies where bores were generally treated as two-dimensional structures examined in a plane normal to the bore. The implementation of a three-dimensional approach to examine the role of bores in generating ascent maintaining or initiating deep convection would be similar to the well-known RKW theory (Rotunno et al., 1988). This theory is utilized to examine how the variations in updraft strength at the leading edge of squall depend on the cold pool strength and the variations in vertical wind shear in the line-normal direction along an arching cold pool. Changes in bore structure and ascent are expected along an arching cold pool over the SNCP given the previously mentioned changes in the strength of the NLLJ and since the magnitude of the vertical shear normal to the bore depends on the orientation of the cold pool. However, to date, only a few studies (e.g., Blake et al., 2017; Chasteen et al., 2019) have focused on understanding how the interplay between cold pools, bores, and the changes in the stability and winds of the ambient environment varies in three-dimensions along an arching cold pool. Thus, an important but underappreciated aspect in investigations of nocturnal convection with forecast implications is in how bores and their impacts on MCSs vary in heterogeneous nocturnal environments.

In this study, we investigate the structure and dynamics of a nocturnal MCS that occurred over SNCP in a heterogeneous environment. Our goal is to reveal how the generation, evolution, and structure of bores vary in this complex environment and how these variations impact the structure and evolution of the MCS. This research is intended to deepen our understanding of bore dynamics and investigate the potential contribution of bores to the maintenance of nocturnal precipitation over China. Given the unique characteristics in the bore structure, movement, and frequency in previous studies over this region (e.g., Zhang, Parsons, Xu, et al., 2020; Zhang et al., 2022), this research will also provide insight into the wide range of interactions possible between bores and MCSs at other locations.

This paper begins in Section 2 with an introduction of the observational data set and an examination of the observations of the MCS and radar fine lines (RFLs) from two radars to provide insight into their spatial and temporal variations. Section 3 provides an overview of the Weather Research and Forecasting (WRF) model simulation of this event with Section 4 describing the dynamics of the simulated atmospheric bores and its roles in MCS maintenance. The genesis of the simulated bore is presented in Section 5 with the findings and broader implications summarized in Section 6.

2. Observation Analysis

2.1. Data

The data utilized for this study included reflectivity measurements taken at 6-min intervals from the operational S-band radars. The radar hardware and software employed in this study are similar to Weather Surveillance Radar-1988 Doppler radars (WSR-88Ds) in the United States (Min et al., 2019). The observations also included surface temperature and pressure measurements with a precision of ∼0.1°C and ∼0.1 hPa, respectively, at 5-min intervals. The wind speed and wind direction were also obtained from the operational surface observing network. The spatial resolution of the network is ∼25-km. These data were processed with quality-controlled procedures that include the climatological limit value test, internal consistency test, and space and time continuity tests.

The radiosonde measurements utilized in this study were taken at the Xuzhou and Sheyang stations for soundings launched at 2000 Local Standard Time (LST). Finally, we note that the ERA5 reanalysis (Hersbach et al., 2018)

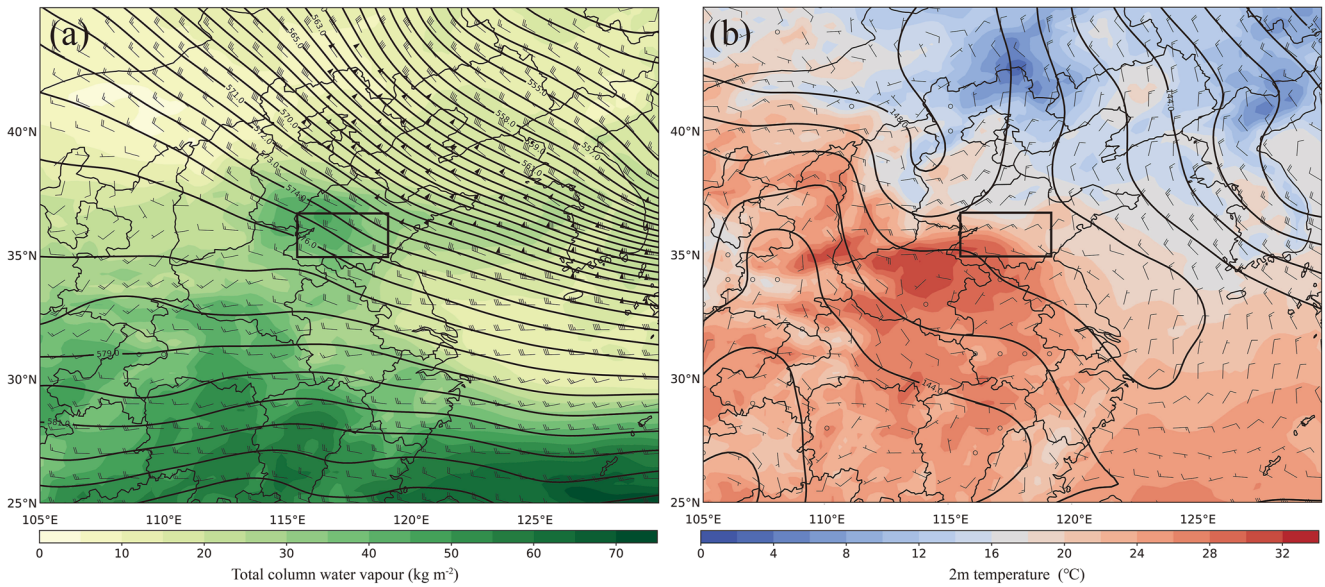

Figure 1. Geopotential height (solid blue contour, ×10 gpm), and wind barbs (one full barb = 10 knots) at (a) 500 hPa with total column water vapor [shaded, kg m^{-2}] and (b) 850 hPa with 2 m temperature [shaded, °C] at 2200 LST on 2 June 2017 derived from ERA5 data. The black rectangle indicates the location of the MCS.

was employed for defining the synoptic conditions over the region. The ERA5 reanalysis is hourly with a spatial resolution of 0.25° × 0.25°.

2.2. Large Scale Environment

We first analyzed the synoptic situation (Figure 1), which had a considerable impact on the evolution of the parent MCS and thus on the associated cold pool whose intrusion into the NSL can generate bores. At 500 hPa (Figure 1a), an upper-level jet was evident with a northwest (NW)-SE orientation with the MCS located south of the jet stream. At 850 hPa, the MCS was located in a region containing confluence with a strong northeasterly wind north and west of the MCS and a weaker flow to the south (Figure 1b). Thus, the location of the MCS was characterized by confluence in the flow at 850 hPa and strong vertical shear between the winds at 850 and 500 hPa. The total column water vapor (Figure 1a) and 2 m temperature (Figure 1b) reveal maxima located to the SW of the MCS, implying a warm and moist environment, which is likely to be conducive for convection initiation (CI). In contrast, the environment to the SE is relative drier and cooler. Hence, the MCS was in a synoptically disturbed and non-uniform environment.

2.3. Radar Observations: Structure of the MCS and Radar Fine Lines

The observations from the Xuzhou (XZ) radar taken during the evening of 2 June 2017 (Figure 2a) show that the MCS originated to the NW over elevated terrain (the Taihang Mountain covering an area of ∼35°–40°N, 110°–116°E) and then moved to the SE during the night (Figure 2b). This evolution is the most common type of MCSs that generates bores over this region (Zhang et al., 2022). At 2230 LST (Figure 2b), the MCS had a relatively complex structure, with an east-west arched RFL stretching for about 200 km on the southern side of the MCS. Intense convective cells were present north of the RFL and on the western edge of the MCS, showing an inverted C-shaped arch. At this time, a broad region with stratiform precipitation (echoes with reflectivity factors from 20 to 40 dBZ as defined in Parker & Johnson, 2000) was located NE of the RFL.

Subsequently, the MCS and associated RFLs were observed by another radar (Huaian [HA] radar) located to the SE of XZ radar revealing different evolution and structure (Figures 2g–2j). The radar observations at XZ station (Figures 2c–2f) indicated that the RFL propagated at a speed of ∼14.2 m s^{-1}, while the propagation direction evolved toward the SW with weak clear-air radar echoes located behind the RFL. During this period, the arched RFL evolved to become less clearly evident as a larger area of convection cells formed within the MCS (Figure 2e) with CI (Figure 2f) taking place behind the leading RFL. The evolution of the MCS with cells forming

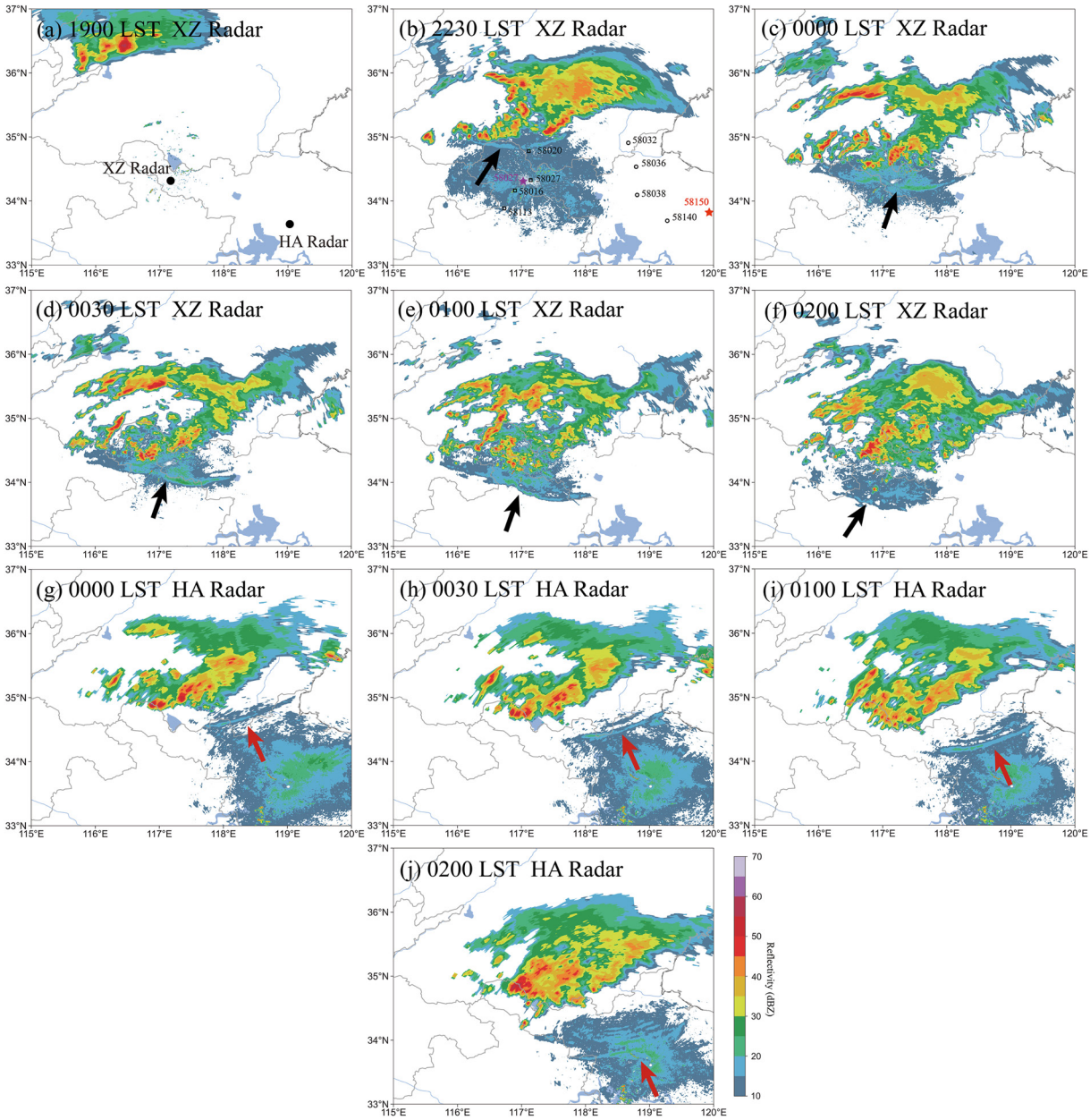

Figure 2. The 0.47° reflectivity plots at XZ radar station at (a) 1900, (b) 2230 LST, depicting the early stage of the MCS; (c) 0000, (d) 0030, (e) 0100, (f) 0200 LST, depicting the evolution of the RFL in the southwest. The 0.47° reflectivity plots at HA radar station at (g) 0000, (h) 0030, (i) 0100, (j) 0200 LST, depicting the evolution of the RFL in the southeast. In (a), the solid circles indicate the locations of the two radars; In (b), the hollow rectangles and circles indicate the locations of the ground-based stations used in Figure 3, the purple and red stars indicate the locations of the radiosonde stations of Xuzhou and Sheyang used in Figure 5. The black and red arrows indicate the locations of the leading edges of RFL(s) to the southwest and southeast, respectively.

behind the RFL implied a discrete propagation of the MCS (Bodine & Rasmussen, 2017; Fovell et al., 2006; Zhang, Parsons, & Wang, 2020) as convection surged ahead of the main body of the MCS in the warm and moist environment to the SW.

As shown in Figures 2g–2j, the radar observations at HA station suggest that multiple RFLs became apparent starting at about 0000 LST with the appearance of an undular bore propagating into a pristine dry and cooler environment. During this time, the parent MCS moved relatively slowly to the SE, while the undular bore indicated by the RFLs propagated more rapidly in that direction. The questions raised by the radar observations in Figure 2 are as follows: (a) Why do the RFL(s) exhibit different evolution to the SW and SE? (b) How do variations in the

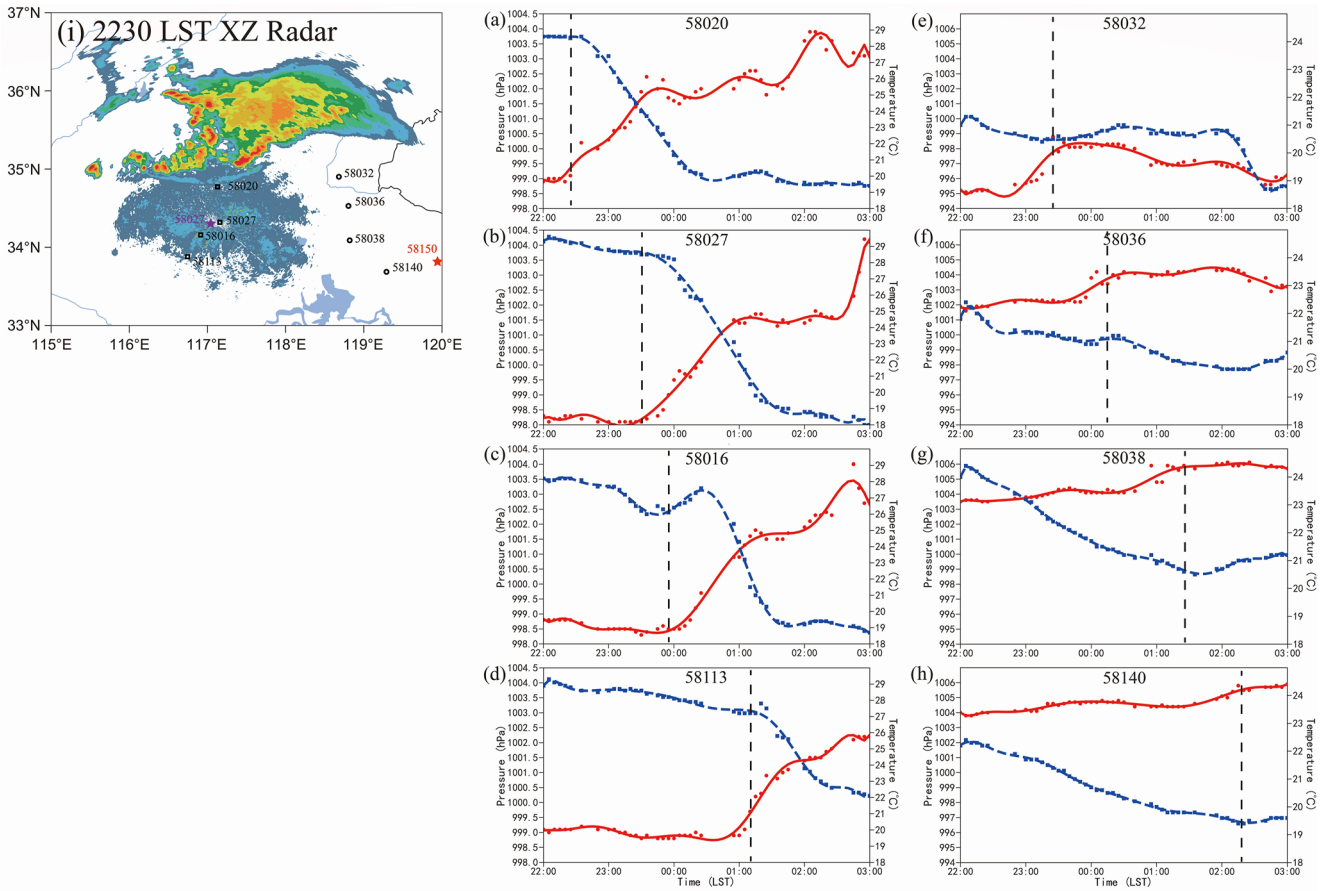

Figure 3. The fitted curves of the temperature (blue dashed line; °C) and pressure series (red solid line; hPa) at selected stations, (a–d) in the southwest and (e–h) southeast. The colored dots indicate the individual data records, the black dashed lines indicate the passage of the observed RFL(s) at different directions, and the locations of the ground-based stations are shown in (i).

environment affect the structure and movement of the cold pool and bores? (c) Do the RFL(s) generated in front of the MCS play an important part in the maintenance of the MCS?

2.4. Surface Observations: Identification of Bores

It is well established that convective outflows associated with cold pools typically cause wind shifts, pressure jumps and pronounced cooling at the surface. However, the impacts of a bore on surface conditions are often less dramatic with only a semi-permanent (~30 min) pressure increase and no temperature change or slight warming at the surface due to the downward mixing of the NSL before the arrival of the residual gravity current or subsequent diabatic cooling (Haghi et al., 2017). Thus, the variations in temperature and pressure along the path of the RFLs can be used to determine the nature of the RFL(s). The surface observations during the time the RFL(s) passed over eight ground-based stations are shown in Figure 3. These stations are located approximately equidistantly along the path of RFL(s) to the SW and SE of the MCS, respectively (locations are shown in Figure 3i). The general evolution of surface observation data is shown by fitted curves (the 12th-degree least squares polynomial fitting) to eliminate missing observations and delineate the impacts of the bores more clearly, such as the apparent increase in temperature.

As the RFL propagated forward, the pressure at each station to the SW (Figures 3a–3d) rose sharply by about 2–3 hPa. The temperature at the stations (58020, 58027) close to the MCS remained relatively stable, while farther to the SW of the MCS the temperature increase was large at station 58016 and slight at the station 58113. As noted earlier, a pressure increases and stable or increasing temperature at the surface is consistent with the passage of a bore. The variations of temperature and pressure captured by the four stations provides insight into

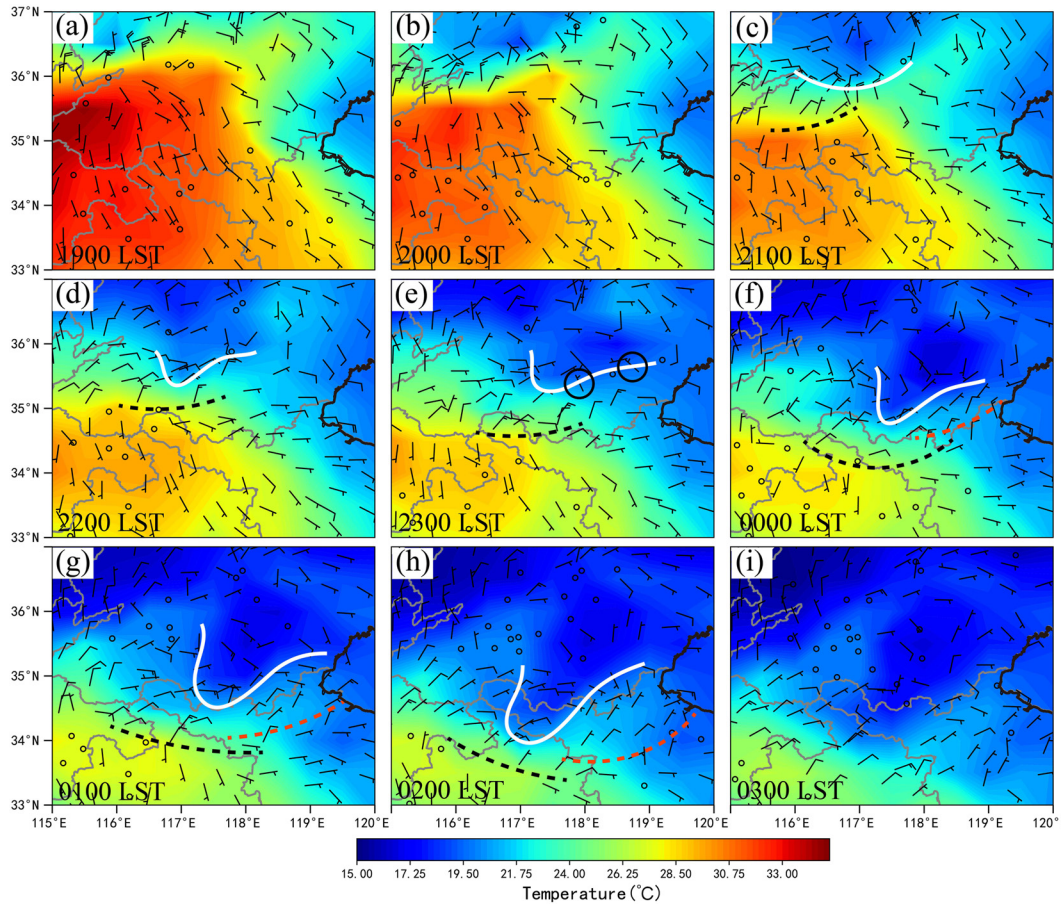

Figure 4. Two-dimensional linear interpolated surface temperature observations (shaded areas; °C), and observed surface wind fields (wind barbs in knots) from (a–i) 1900 LST on June 2 to 0300 LST on 3 June 2017 at 1-hour time interval. Sold white lines indicate the leading edge of the cold pool with a maximum temperature gradient. Dashed black (red) lines indicate the locations of the leading edge of the RFLs captured by XZ and HA radar in the southwest and southeast, respectively. The black circles in (e) indicates the location of the stations with northwesterly wind shift. The thick black lines denote the coastline.

the evolution and structure of the bore with the formation of the bore detected by stations 58020 and 58027, the evolution subsequently observed by station 58016, and finally the dissipation revealed by station 58113. All four stations of these stations experienced a sustained pressure rise with a sharp temperature decrease after the warming associated with bores, indicative of the passages of a bore with a following cold pool. At the stations to the SE (Figures 3e–3h), the variations of pressure and temperature were similar but with smaller increases indicating a weaker signal from the undular bore with temperature increments of 0–1°C and 0–0.5°C at the stations to the SW and SE, respectively. At the stations to the SE, the sharp increase in pressure and decrease in the temperature after the passage of the bore were missing, implying the absence of a cold pool. Another difference in the bore structure to the SE is that the pressure increase occurs far earlier than the temperature increases implying that the downward mixing of warm air often associated with a bore did not occur at the leading edge of the bore.

2.5. Bores Generated in the Non-Uniform Environment

The surface analysis (Figure 4) shows the evolution of surface temperature and wind helping to illustrate the underlying mechanism for the generation of the bores, especially to the SW. A non-uniform ambient environment is clearly evident with a cooler air mass along the coast. These variations are a common phenomenon at night during the warm season in this region due to the presence of the predominantly SE wind from the Pacific subtropical high, and at times, a local sea breeze (Huang et al., 2016). A warmer air mass is located inland with a dominant southerly wind, which is nearly perpendicular to the extension of the MCS to the SW providing a potentially favorable environment for convection initiation.

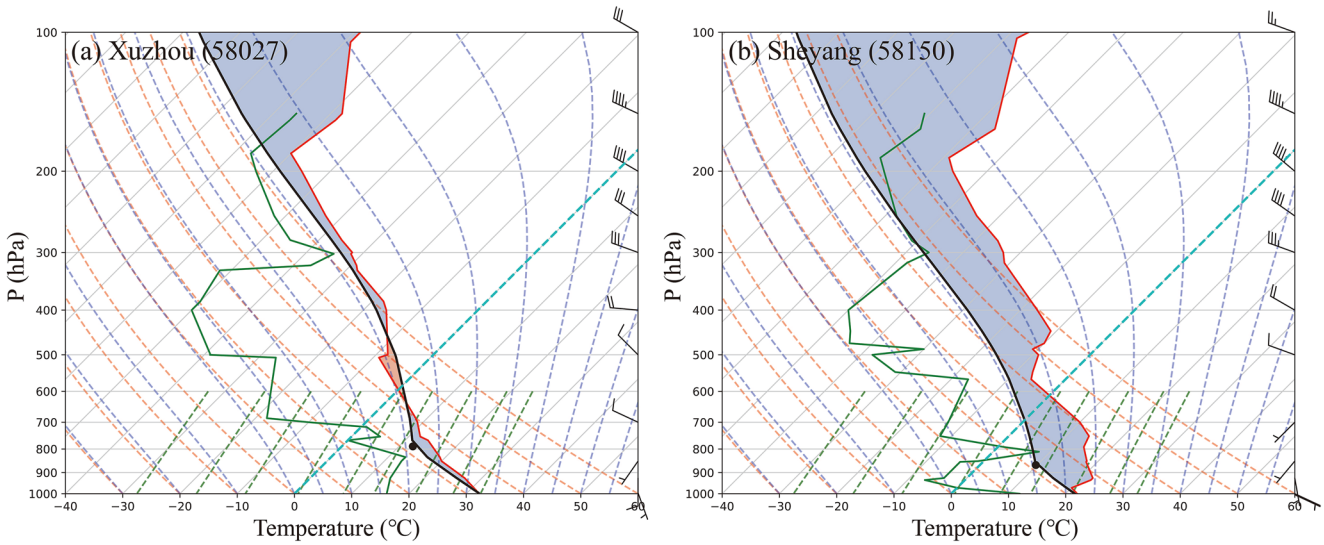

Figure 5. Sounding data at 2000 LST from the radiosonde station (a) Xuzhou to the southwest of the MCS and (b) Sheyang to the southeast. The ambient temperature and dewpoint are represented by the solid red and green lines, respectively. The parcel that ascends undiluted from the surface is shown by the dashed black curve. Half and full barbs denote 2 and 4 m s^{-1}, respectively. The convective inhibition (CIN) area is shaded light blue and the convective available potential energy (CAPE) area is shaded light orange.

Examining the evolution of the MCS in this environment, a cold pool extended to the south and SW from the MCS and was accompanied a northeasterly wind and a maximum temperature gradient at its leading edge indicated by solid white lines in Figure 4. These observations also corresponded well to the evolution of the MCS and RFLs revealed in Figure 2 that showed the MCS extending to the SW. As the MCS evolved toward midnight (Figures 4b–4f), the boundaries (dashed black lines) consistent with the RFLs propagated away from the MCS, but with a gradually weaker temperature gradient implying the formation of the bore from a gust front at earlier time (Figure 4c). This weakening of the cold pool and the formation of a bore is consistent with the ambient environment cooling and stabilizing due to nocturnal radiative processes. Consistent with the surface and radar observations along with numerous studies referenced earlier, one can conclude that the formation of the bores to the SW that was captured by Xuzhou radar was likely due to the intrusion of a cold pool into the NSL.

However, to the SE of the MCS, the leading edge of the boundaries (indicated by dashed red line) took on the appearance of an undular bore in the radar data that subsequently propagated into the cooler air mass along the coast (Figures 4f–4h). Given the relatively small temperature difference between cold pool and ambient environment and the weak low-level NW winds, the intruding cold pool located behind the bore to the SE was rather weak and moved quite slowly in this direction, as shown in the east portion of the white lines in Figure 4. The evolution of the flow was more complex to the SE of the MCS than the to the SW as the two stations at the SE boundary of the cold pool experienced a wind shift from NE to NW ∼ 1 hr before the undular bore generated (Figure 4e). This evolution implies a more complex generation of the undular bore than the cold pool generated bore to the SW and the cold pool generated noted in past studies. The mechanism for the bore generation will subsequently be investigated using our numerical simulations.

The sounding data taken at 2000 LST further reveals considerable variations in the thermodynamical environment ahead of the MCS (Figure 5). The soundings were taken prior to the generation of the bores and the reader should note that nocturnal boundary layer is likely to further stabilize. The sounding taken from Xuzhou radar to the SW of the MCS suggests nearly constant values of potential temperature and water vapor extending from the surface to ∼850 hPa, implying a well-mixed layer (Figure 5a). In the Xuzhou sounding, the middle levels were dry with weak wind shear between 400 and 850 hPa and strong NW winds aloft. Weak Convective Available Potential Energy (CAPE) also existed (∼123 J kg^{-1}) with a level of free convection (LFC) at ∼650 hPa. Thus, the environment to the SW of the MCS was conducive for deep convection if the lifting was enabled parcels to reach their LFC. In contrast, the flows to the SE revealed by the Sheyang radiosonde station (Figure 5b) were characterized by a cooler and more intense NSL with dry upper layers and near-zero CAPE. A nearly well-mixed layer was also evident above the NSL extending from ∼750 to ∼550 hPa. The wind profiles also showed a greater

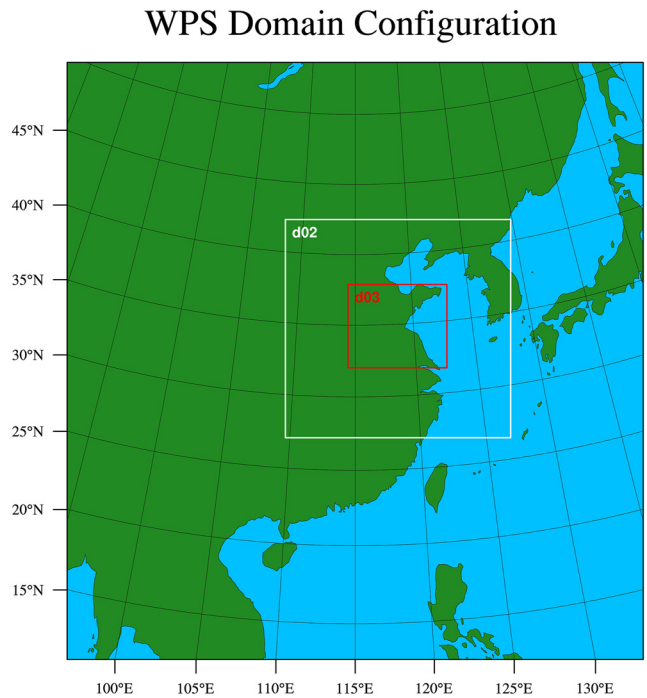

Figure 6. Domains of the WRF model used in this study. The horizontal grid spacing of the outer domain is 9 km, and the two inner domains represented by d02 and d03 have resolutions of 3 and 1 km.

surface inflow toward the MCS from SE. The differences in the sounding data were consistent with the surface situation described earlier (Figure 4) and provide a possible explanation why CI occurred in the SW rather than to the SE.

3. Numerical Simulation

A numerical simulation of the MCS was conducted to investigate how the structure of convective outflows and bores varied and evolved in this non-uniform baroclinic environment. The use of a simulation has significant advantages to understand the evolution of the MCS and the generation of the bores relative to the observations given the frequency of the sounding measurements. This knowledge of the detailed evolution of the convective outflows and bores was also utilized to determine the roles of bores and convective outflows in the maintenance, structure, and evolution of the MCS.

3.1. Experiment Design

The MCS was simulated using the WRF-Advanced Research WRF (WRF-ARW version 4.0) model (Skamarock et al., 2008). The simulation was carried out for 24 hr starting at 1800 LST on 1 June 2017 using three two-way nested domains with horizontal resolutions of 9 km, 3 and 1 km (Figure 6). In the vertical, 49 levels were employed with the grid spacing varying from ~60 m near the surface to ~300 m toward the model top near 17 km. Table 1 provides the configurations of the model physics. The initial and boundary conditions, with a resolution of 0.25° × 0.25°, were derived from the 6-hourly NCEP GDAS/FNL Global Tropospheric analyses.

3.2. Evaluation of the Model Simulation

Comparisons with the radar observations (Figure 2) show that the WRF model generally captured the nature of the MCS (Figure 7). Specifically, the model reproduced the general structure of the MCS with a bow-shaped

Table 1
Summary of the ARW Configuration for This Study

Attribute	Domain #1	Domain #2	Domain #3	References
Grid spacing	9 km	3 km	1 km	
Horizontal dimensions	4590 km × 4,428 km	1,677 km × 1,731 km	640 km × 760 km	
Vertical sigma levels	49	49	49	
Model top pressure	50 hPa	50 hPa	50 hPa	
ICs and LBCs	FNL-0.25°	FNL-0.25°	FNL-0.25°	
Microphysics	Morrison 2-moment	Morrison 2-moment	Morrison 2-moment	Morrison et al. (2005)
Longwave radiation	CAM	CAM	CAM	Collins et al. (2004)
Shortwave radiation	CAM	CAM	CAM	Collins et al. (2004)
Surface layer	Pleim-Xiu	Pleim-Xiu	Pleim-Xiu	Pleim (2006)
Land surface model	Pleim-Xiu	Pleim-Xiu	Pleim-Xiu	Pleim (2006)
Boundary layer physics	Asymmetrical Convective Model version 2	Asymmetrical Convective Model version 2	Asymmetrical Convective Model version 2	Pleim (2007)
Cumulus parameterization	Kain-Fritsch	None	None	Kain (2004)

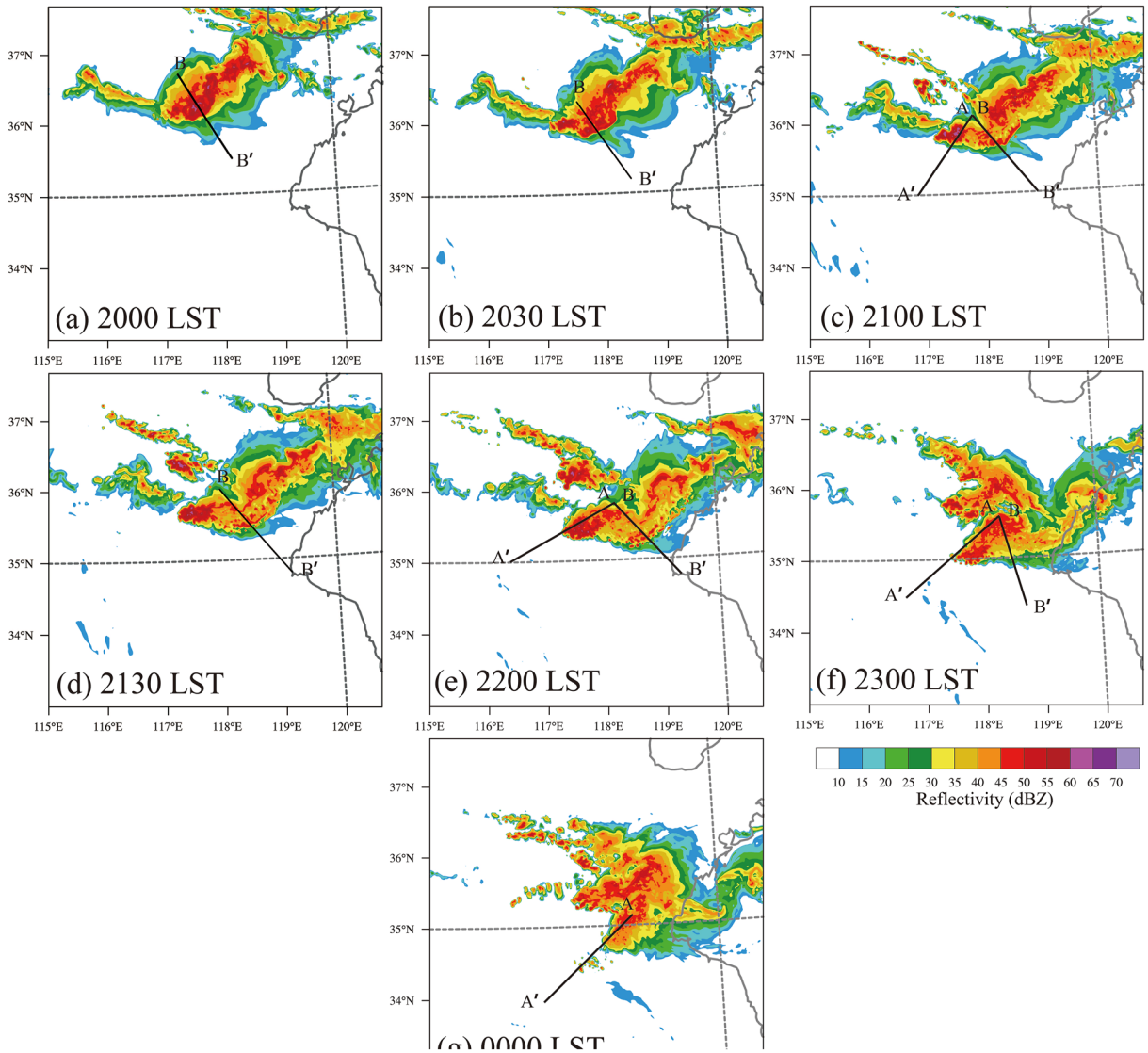

Figure 7. Composite reflectivity (dBZ) simulated by the WRF model at the 1-km resolution at (a) 2000 LST, (b) 2030 LST, (c) 2100 LST, (d) 2130 LST, (e) 2200 LST, (f) 2300 LST, and (g) 0000 LST. The black line labeled by A, A′, B, and B′ indicate the paths of the vertical cross-section in Figures 10 and 11, respectively, at the corresponding time.

echo. The model also captured the overall evolution of the MCS with an expansion of the MCS to the SW due to CI ahead of the MCS and a more stagnant MCS to the SE (Figure 7g). However, the position of the simulated MCS was found to deviate somewhat to the NE of the observed system and this difference is common in simulations of observed convective systems (Davis & Galarneau, 2009; Meng et al., 2013; Zhang, Parsons, Xu, et al., 2020). The area with reflectivity greater than 40 dBZ was broader in the simulation than the observations with far stronger and more extensive convection extending westward (see the several branches of strong in Figure 7g). This difference is consistent with known problems on diagnosing precipitation properties in microphysical parameterizations (Morrison & Milbrandt, 2015).

The vertical velocity at 1 km above ground level (AGL) in the model simulations indicates that in the early stage of the MCS evolution at 2100 LST (Figure 8a) there was a single band of ascent in front of the system. The bands of vertical motion and the associated reflectivity pattern changed from a well-defined bow echo (Figure 8a) to two separate segments each with an undular pattern of ascent (Figure 8b). The evolution to an undular pattern (Figures 8b and 8c) is similar to the observed system (Figure 2). This undular pattern in the simulations propagated ahead of the MCS at a speed of ~13.8 m s^{-1} which is also comparable to the observations. The general

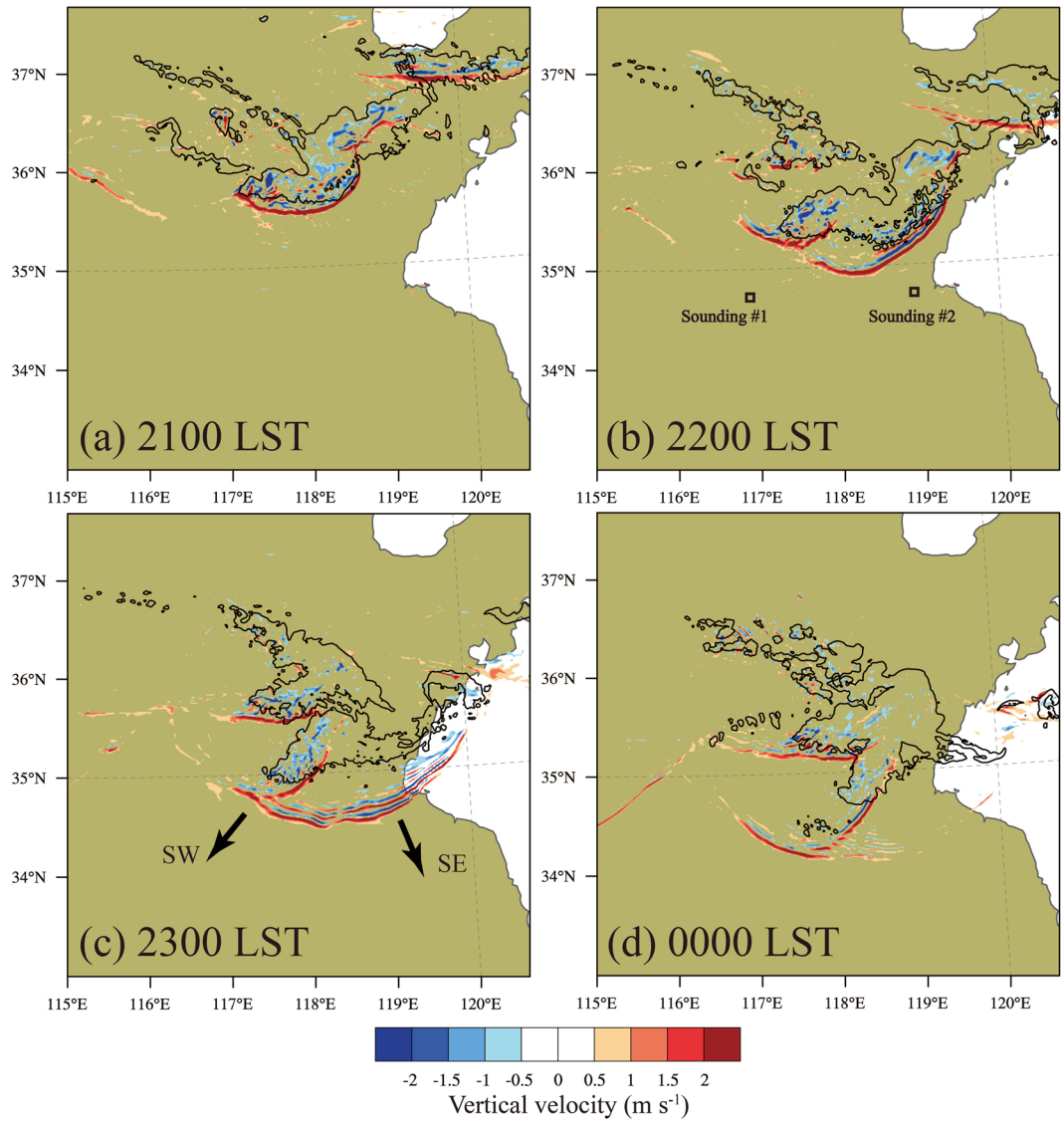

Figure 8. Vertical velocity (shaded areas; m s^{-1}) at 1 km AGL and composite reflectivity of 35 dBZ (black contours) simulated by the WRF model in the 1-km-resolution domain at (a) 2100, (b) 2200, (c) 2300, and (d) 0000 LST. The hollow rectangles indicate the regions where to derive the vertical profiles in Figure 10. The land is colored dark khaki. The arrows labeled SW and SE indicate the separative directions of the evolution of the MCS and bores.

evolution of the vertical velocities from a single to multiple bands of ascent is consistent with the formation of undular bores with differences between the SW and SE directions as was found in the observations (Figure 2). To the SW, the western portion of the MCS developed and extended to the SW with CI occurring behind the leading edge of the undular disturbances (Figure 8d). This CI caused discrete propagation of the MCS similar to past studies (Fovell et al., 2006; Zhang, Parsons, & Wang, 2020; Zhang, Parsons, Xu, et al., 2020). To the SE, the eastern portion of the MCS stagnated (Figure 8c) with an appearance consistent with an undular bore ahead of the MCS. As expect from the more stable environment, the undular bores failed to initiate convection to the SE at 0000 LST (Figure 8d).

The most unstable CAPE (MUCAPE) in the layers from surface to the LFC, the temperature, and wind fields are shown in Figure 9. To the west and SW of the MCS, a broad region with large MUCAPE which favors CI was evident (Figure 9a), but varied in space with a maximum to the west. Although the simulated MUCAPE was larger than in the observational soundings (Figure 5), the overall characteristics of ambient environment were relatively well represented as can be seen from comparing Figures 5 and 10. The evolution of the simulated

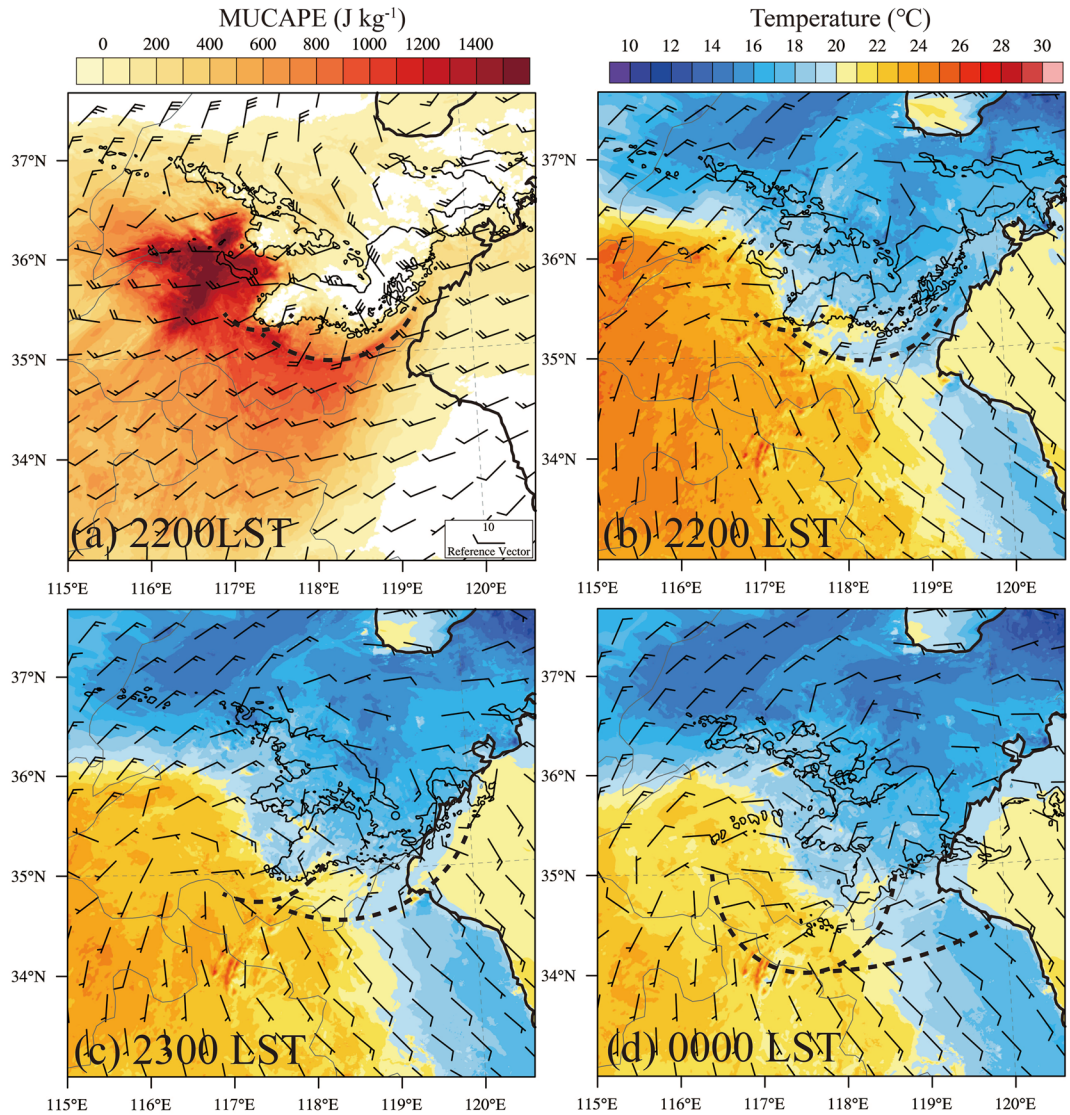

Figure 9. (a) The simulated most unstable CAPE (MUCAPE; shaded areas; J kg^{-1}), 1.5 km total wind field (wind barbs in knots) above mean sea level (MSL) at 2200 LST. The simulated surface temperature at 2 m MSL (shaded areas; °C) and surface total wind field at 10 m MSL (wind barbs in knots) at (b) 2200, (c) 2300, and (d) 0000 LST. The black dashed lines indicate the locations of the leading edge of the upward disturbances in Figure 8, and the thick black lines denote the coastline.

surface temperature and wind (Figures 9b–9d) are also consistent with the observations (Figure 4). Specifically, there is an inland warm air mass with cooling owing to radiative process with south and southeasterly winds at the surface and a cooler air mass along the coast with southeasterly winds. There was also a 180° wind shift (oscillations) between the portions of undular bores (indicated by dashed black line) and the low-level inflow. However, the wind shift does not coincide with a drop in temperature consistent with the observed cold pool and bore structures.

The simulated vertical profiles (Figure 10) are derived from the region's mean of 10 × 10 km squares situated to the SW and SE of the MCS. These calculations are performed at 2200 LST, the time when the bores are about to develop. The results once again demonstrate strong agreement with the observations (Figure 5), except for the formation of a shallow stable boundary to the SW (Figure 10a), which is likely attributed, in part, to the continued radiation cooling during late night. The inhomogeneity between the two environments is also evident in the soundings (Figures 10a and 10b), as for example, in the different attributes of the surface inversions and the

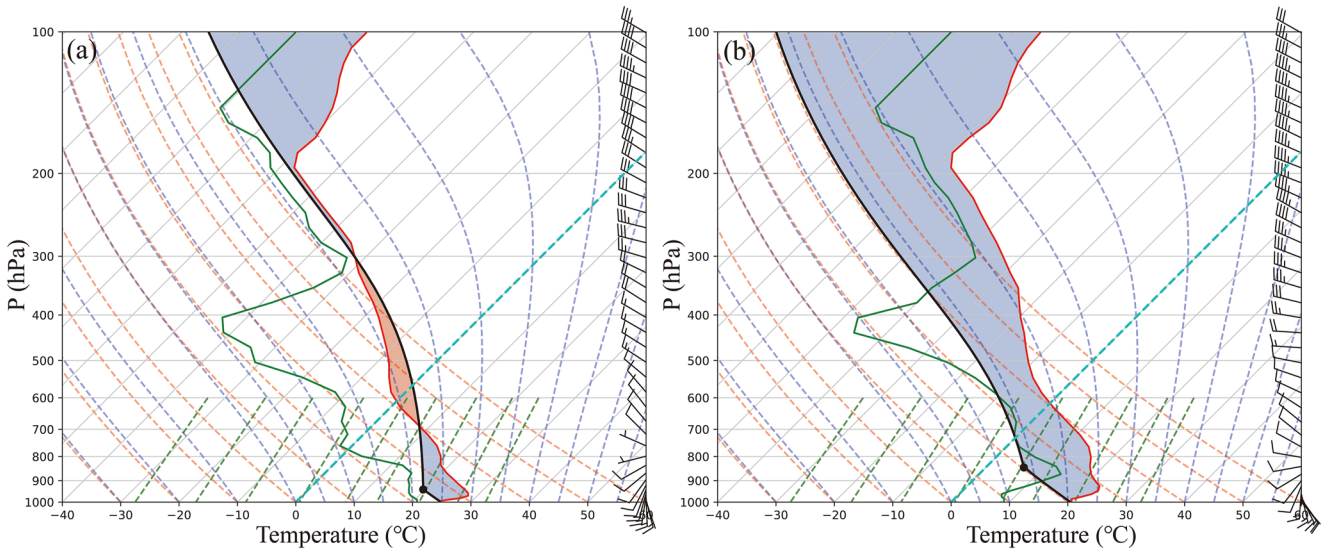

Figure 10. Same as Figure 5, but for simulated vertical profiles at 2200 LST derived from the area located (a) southwest and (b) southeast to the MCS.

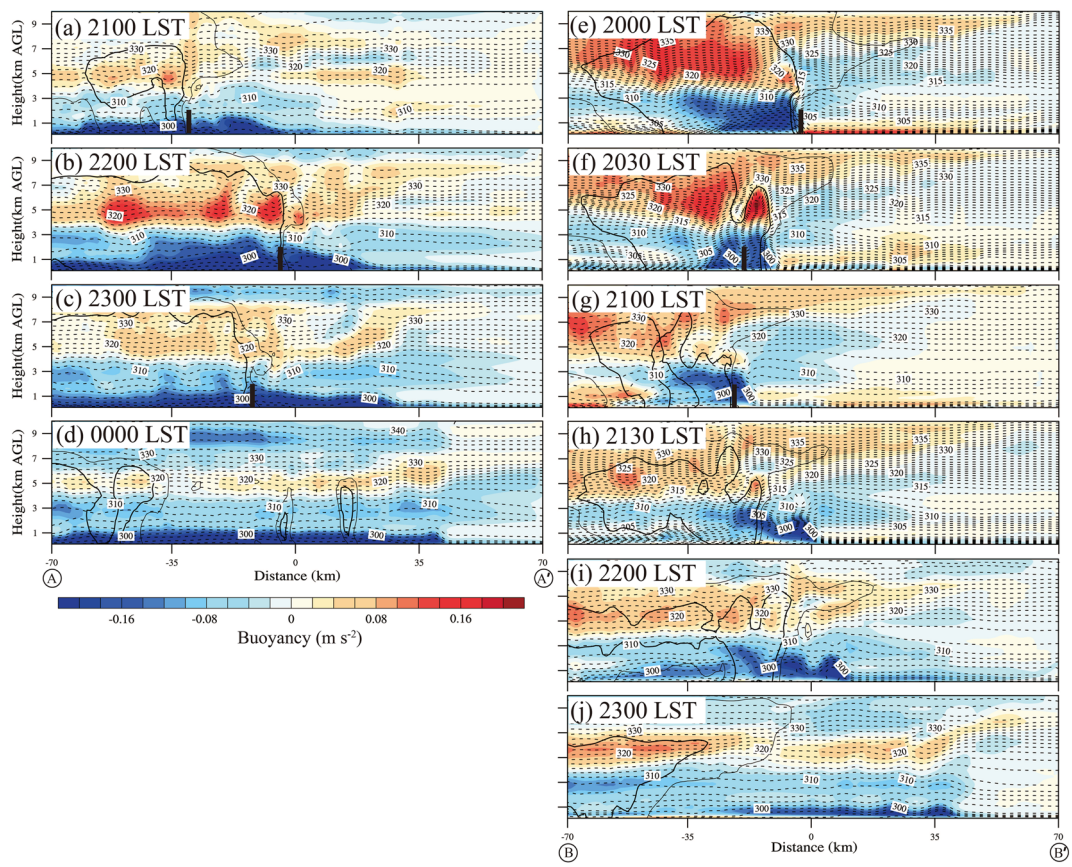

Figure 11. The height-distance cross sections of the buoyancy, B, (shaded areas; m s^{-1}) and potential temperature, θ, (dashed line; K) in the 1-km-resolution domain perpendicular to the leading front of the undular disturbance (a–d) in the southwest (lines A and A′ in Figure 7) and (e–j) in the southeast (lines B and B′ in Figure 7). The contours represent reflectivity of 15 dBZ (thin black lines) and 35 dBZ (thick black lines). The black bars indicate the leading edge of the cold pool whenever is identifiable (corresponding to the sharp decreases in surface temperature). Note that the leading front of the MCS is positioned near the middle of these cross sections, labeled by "0."

thermodynamic conditions at mid-levels. Overall, the simulation appeared to well capture the structure, evolution of the MCS and the variations in the ambient environment.

4. Dynamics of the Simulated Atmospheric Bore and Its Role in MCS Maintenance

In this section, we explore the spatial variation in the dynamics and thermodynamics of the undular bores within the simulation.

4.1. Thermodynamic Structures of the Atmospheric Bore

The buoyancy field (B) within vertical planes perpendicular to the SW and SE portions of the bore in Figure 11, was calculated by using Equation 1 as described in past studies (e.g., Adams-Selin & Johnson, 2013; Zhang, Parsons, Xu, et al., 2020),

$$B \equiv g\left[\frac{\theta'}{\overline{\theta}} + 0.61\left(q_v - \overline{q}_v\right) - q_c - q_r - q_i\right], \tag{1}$$

where g denotes the gravitational acceleration, $\overline{\theta}$ and $\overline{q}_v$ represent the potential temperature and water vapor mixing ratio of the ambient air ahead of the gravity current, respectively. Within the MCS, θ' represents the deviation in θ from $\overline{\theta}$, q_c indicates the cloud water mixing ratio, q_r the rainwater mixing ratio, and q_i the mixing ratio of frozen condensation. The terms in the buoyancy equation are calculated as a function of height in relation to a reference ambient air mass within the 1-km-resolution model domain at a location ∼20 km ahead of the leading edge of the updraft disturbances shown in Figure 8. The air mass characteristics in the ambient environment were calculated as a function of the height and time using a 5 km × 5 km horizontal box.

Figure 11 shows the vertical cross-sections of the perturbation in buoyancy and potential temperature to depict the evolution and structure of the bores, cold pools, and the ambient environment. Ahead of the portion of the MCS to the SW (Figures 11a–11d), the stability of the NSL in front of the MCS was weak with an estimated depth of about 500 m, the top of which was defined as the level at which $d\theta/dz$ first drops below 0.005 K m^{-1}. The ambient environment above that level were generally mixed, with the layers between 0.5 and 1.5 km having a constant potential temperature. A layer between ∼1 km and 5 km in height on the x-axis ranging from 10 to 70 km showed weak positive buoyancy (Figure 11a), consistent with the warm and moist environment reflected by the sounding data (Figure 10a). This weakly unstable layer subsequently became stable, possibly due to the lifting of the low-level inversion by the bore (referring to the leading edge of the negative buoyancy of bores around ∼5 km on x-axis), differential advection, or radiative process in front of the MCS (Figures 11b–11d). The buoyancy distribution was similar to that in the MCS study over the SNCP (Zhang, Parsons, Xu, et al., 2020). However, the environment differs substantially from studies over the Great Plains of North America (e.g., Parsons et al., 2019; Zhang, Parsons, & Wang, 2020) which often contains pronounced positive buoyancy aloft near the top of the NSL associated with the transport of warm and moist air from the south by the NLLJ. This transport can occur over the Plains of North America is typically due to synoptic forcing or more commonly well-known formation of a NLLJ due in part to the thermal variations associated with sloped terrain.

At 2100 LST in the SW portion of the MCS (Figure 11a), a shallow layer of surface negative buoyancy was located within and ahead of the leading edge of the MCS, with the cold pool confined to within the MCS and bores located ahead of the MCS. The negative buoyancy associated with the cold pool became substantially stronger as the MCS developed (Figure 11b) with the depth of the cold air outflow ranging from about 1.2 km to nearly 3 km. At this time, there was also a more pronounced separation of the cold pool and bore implying the generation of the bore in front of the cold pool. Subsequently, at 2300 and 0000 LST (Figures 11c and 11d), the negative buoyancy associated with the bore moved further ahead of the MCS as the scattered CI occurred after its passage (Figures 8d, 9d, and 11d). During this time, the cold pool became even shallower and difficult to distinguish from the bore. This evolution of the negative buoyancy field is consistent with the formation of a bore due to the intrusion of a cold pool, and similar to the findings in Zhang, Parsons, Xu, et al. (2020), implying weaker cold pools are likely occur in the moist environment over SNCP, compared to their counterparts over the Great Plains of the United States. At higher levels within the MCS (4–7 km), positive buoyancy was evident, indicating elevated convection within the MCS as has been found in case studies of events over both the SNCP and the Great Plains (e.g., Blake et al., 2017; Zhang, Parsons, & Wang, 2020; Zhang, Parsons, Xu, et al., 2020).

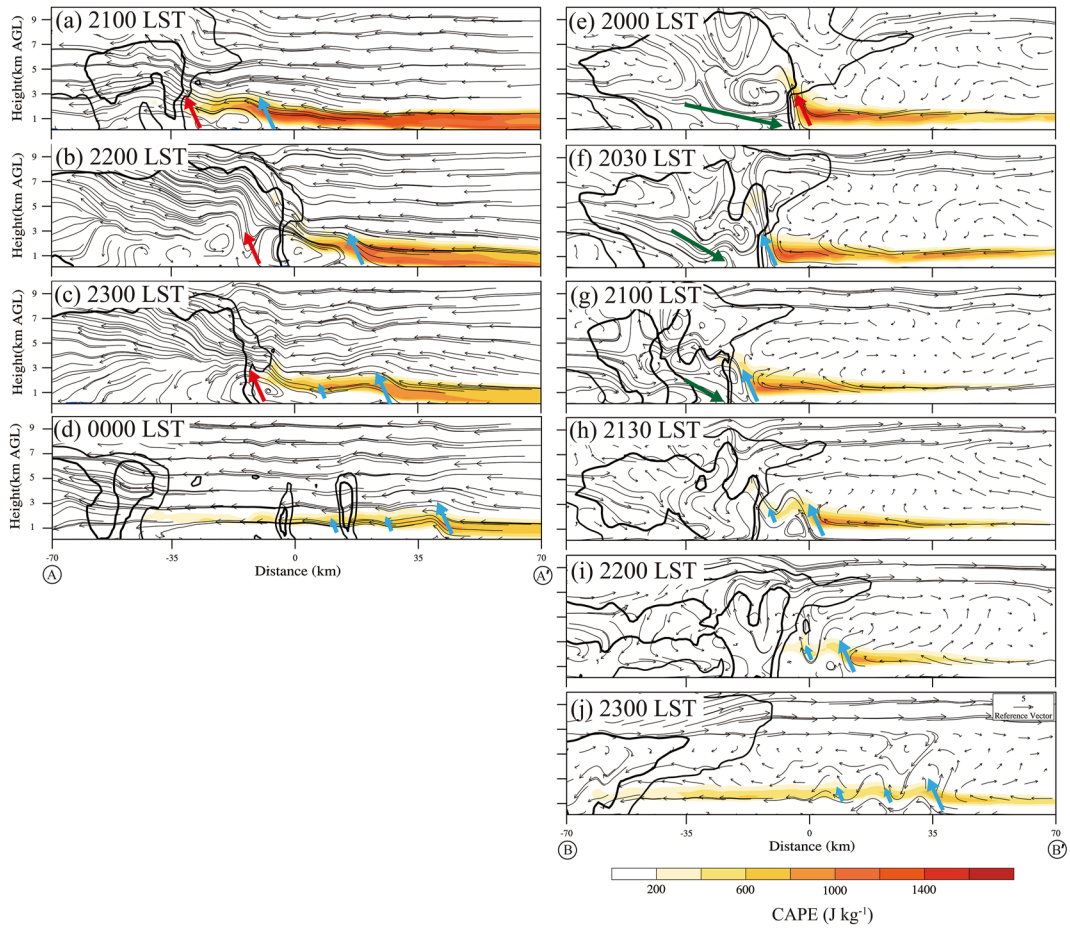

Figure 12. Same as Figure 11, but for the CAPE (shaded areas; J kg^{-1}), and the storm-relative flow (streamlines with vertical velocity multiplied by 5). The red and blue arrows indicate the locations of the cold pool and bore lifting, respectively. The green arrow indicates the location of strong downdraft.

In contrast, in the region SE of the MCS (Figures 11e–11j) an area of negative buoyancy was found within the MCS with a completely different pattern from its counterpart to the SW. At 2000 LST (Figure 11e), the negative buoyancy was initially concentrated in the front of the MCS covering a depth of more than 3 km slanting backward and merging with the low-level rear-to-front flow (Figure 12e). Referring to Figures 11e and 12e, it is apparent that a downdraft associated with convection at the leading edge of the MCS has formed and reached to the surface, but a bore has not been generated at this time. This pattern of strong negative buoyancy linked to the rear-to-front flow is typically associated with water loading, melting and evaporation leading to a mesoscale downdraft within the MCS (e.g., Young et al., 1995). At 2030 LST (Figure 11f), the slanting area of negative buoyancy has transitioned into two smaller areas with large negative buoyancy at the leading edge of the system. The negative buoyancy at the leading edge of the MCS is associated with localized convection as shown by an area of positively buoyant air above negative buoyancy. At 2100 LST (Figure 11g), the negative buoyancy associated with the leading edge of the bore portion has propagated forward with a dramatic weakening of the cold pool with the negative buoyancy taking on the appearance of an undular bore at 2130–2200 LST as shown in Figures 11h and 11i. The existence of a bore forming as a result of a mesoscale downdraft at the leading edge of an MCS has not been observed in previous studies. Subsequently, the undular bore propagated forward at a faster speed than the MCS and gradually became weak (Figure 11j).

The variations in the MCS and bore structure between the SW and SE direction is consistent with the difference between the environment as to the SE, the NSL was more robust with larger increases in the potential temperature with height (Figure 11). The depth of the stable layer increased from about 800 m at 2100 LST to about 1 km at 2200 LST. This increase in the depth and magnitude of the NSL to the SE and the negative buoyancy associated with the strong downdraft likely played an essential role in the formation of the undular bore.

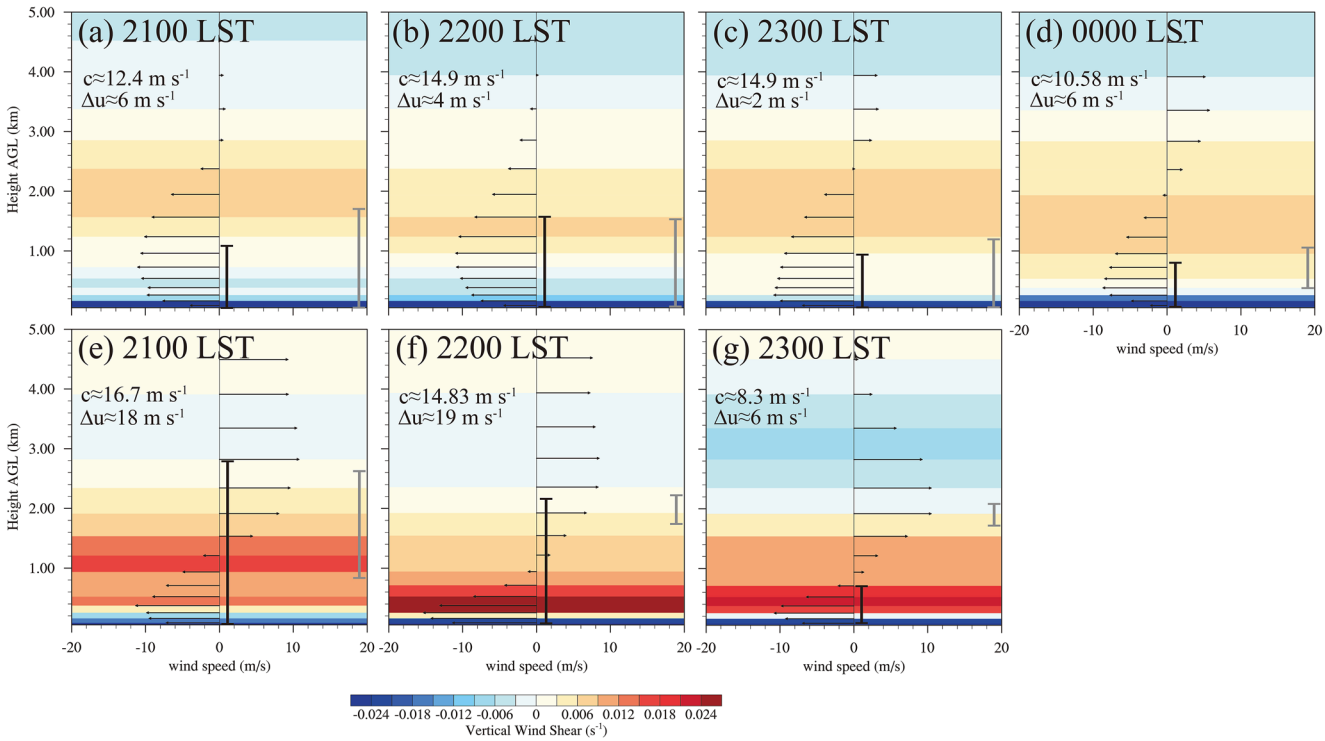

Figure 13. Vertical profiles of the horizontal ambient wind velocity (arrows; m s^{-1}) in the (a–d) southwest and (e–g) southeast within the vertical plane of Figure 11. The colored contours denote the vertical wind shear (s^{-1}) in the background, and the black and gray segments indicate the layer of the cold pool/bore and maximum CAPE, respectively.

4.2. Impact of the Undular Bore on the Maintenance and Structure of the MCS

In this section, we investigate how the bore and its surrounding environment affect the maintenance and structure of the MCS. In the region to the SW of the MCS (Figures 12a–12d), there was a region of large CAPE within and above the NSL with the low-level flow moving into the MCS. This large CAPE decreases as the MCS evolved later in the night consistent with radiational cooling. The bore ahead of the MCS and the subsequent cold pool substantially lifted the flow associated with this large CAPE to a height of about 3 km with the large CAPE air then entering into the MCS (Figures 12a and 12b). This lifting of the flow with large CAPE contributed to the maintenance of the MCS. This finding is also confirmed by the convective cell initiated in lower levels ahead of the MCS in Figure 12a. As the bore propagated forward ahead of the MCS (Figure 12c), the low-level airflow with large CAPE was lifted by the bore to about 1.5 km. Subsequently, the airflow moved into the MCS and was lifted again by the cold pool. This phenomenon of lifting by a bore and then by the cold pool of the MCS was also found by Blake et al. (2017).

At 0000 LST (Figure 12d), as the bore continued to move forward with several weak undular oscillations trailing behind (again, consistent with the observations in Figures 2d–2f), the cold pool started to dissipate and weaken, individual convective cells appeared behind the bore and with some long-lived cells merging into the MCS even as the ambient CAPE values also decreased. This evolution leads to discrete propagation of the MCS (Fovell et al., 2006) as shown earlier in the observations. The lifting by the bore will also decrease of Convective Inhibition (CIN) which is also significant factor in CI (Koch, Feltz, et al., 2008; Koch, Flamant, et al., 2008). To the SW, the stable boundary layer consistent with CIN is confined within the lowest layers in NBL (Figures 11a–11d) and the lifting by the bore above this height, suggests a conducive environment for the elevated CI.

In contrast, along the SE portion of the MCS, the strong slope of the downdraft around 4 km in height lifted and transported air with large CAPE into the MCS (Figure 12e). Hence, the strong subsequent lifting of the large CAPE flow by the formation of the bore contributed to CI (Figure 12f). The undular nature of the bore and its lifting continued to strengthen with time, especially at its leading edge, with steeply sloped updrafts lifting air up to 5 km (Figure 12j). This deep lifting by bores is unique and different from its Great Plains counterparts, possibly due to the favorable environmental with deep vertical shear (Figure 13). However, CI subsequently failed

to occur (Figure 12g) as expected, due to the weaker ambient CAPE and larger elevated stable layer shown in Figures 11e–11j consistent with large CIN (not shown).

The RKW theory proposed by Rotunno et al. (1988) reveals that the ideal circumstances for vertical updrafts along outflow boundaries occur when the negative horizontal vorticity ($\boldsymbol{c}$) associated with the MCS is balanced by the positive horizontal vorticity of the ambient vertical wind shear ($\Delta\boldsymbol{u}$). This horizontal vorticity balance can also be applied to bores where the negative horizontal vorticity is produced baroclinically by the cold pool (or the bore in this study) and can be expressed as $\boldsymbol{c} = \sqrt{-\boldsymbol{B}_{\mathbf{min}} \cdot \boldsymbol{H}}$, where $\boldsymbol{B}_{min}$ and $\boldsymbol{H}$ indicate the minimum buoyancy and height of the bore, respectively (Bryan & Rotunno, 2014). Based on this, $\boldsymbol{c}$ and $\Delta\boldsymbol{u}$ were calculated in both the SW and SE (Figure 13). The results demonstrated that in the SW, $\boldsymbol{c}$ is considerably greater than $\Delta\boldsymbol{u}$, indicating that cold pool/bore circulations prevailed over the ambient shear, and the updraft tilted upshear, as shown in Figures 12a–12d. To the SE, $\boldsymbol{c}$ and $\Delta\boldsymbol{u}$ are comparable, suggesting an optimal state of the vertical updrafts and corresponding well to the updrafts shown in Figure 12i. This balance of $\boldsymbol{c}$ and $\Delta\boldsymbol{u}$ is indeed favorable for convection since it leads to deeper and stronger warm air lifting at the leading edge of the cold pool/bore (Parsons, 1992). However, due to the small/greater magnitude of the CAPE/CIN and the mismatch between the lifting and the layer of high CAPE, CI failed to form to the SE at 2300 LST (Figure 13g).

These results indicate that complex interactions, which produce varying impacts that act on different temporal and spatial scales, can influence the intensity and duration of convective systems. These factors include spatial and temporal variations in the magnitudes of the CAPE, convective inhibition, mid-level humidity, distribution of diabatic sources within convective systems, and deep vertical shear (Coniglio et al., 2012; Stensurd et al., 2005). The impact of $\boldsymbol{c}$ and $\Delta\boldsymbol{u}$ on the MCS structure are also evident in both the SW and SE directions. For example, to the SW where $\boldsymbol{c}$ is considerably greater than $\Delta\boldsymbol{u}$, a cold pool or bore circulation occurred with trailing stratiform precipitation (presented in Figure 12a, and outside the image range in panel c), while to the SE where $\boldsymbol{c}$ is comparable to $\Delta\boldsymbol{u}$, a shear dominated circulation occurred with the convection and stratiform precipitation tilting upstream (Figure 12j). The low-level jet is also evident in the SE, providing a favorable situation for bore propagating at a longer distance.

5. Genesis of the Atmospheric Bore

5.1. Classic Hydraulic Theory

In the classic hydraulic theory, shallow-water equations are frequently employed in bore dynamic analysis, approximating the environment as a two-layer, inviscid flow over an obstruction (e.g., Baines, 1984; Baines & Davies, 1980; Houghton & Kasahara, 1968; Long, 1954; Rottman & Simpson, 1989). In this classic theory, the Froude number ($\boldsymbol{F}_r$) and a non-dimensional depth ($\boldsymbol{D}_0$) define four flow regimes, including completely and partially blocked flow regimes that allow bores to form and move upstream of the obstacle (cold pool) (see Figure 9 of Rottman & Simpson, 1989). Additionally, Rottman and Simpson (1989) proposed three types of bores (type A, B and C) of different structures depending on the bore strength defined as $h_1(h_o)^{-1}$; the ratio of the stable layer depth after the bore passage to that prior to the arrival of the bore. Among these bore types, an undular bore of type B was found in a regime where bore strength is greater than 2 but less than 4, with some mixing just downstream of the leading undulation (see Figure 3 in Rottman & Simpson, 1989). In this application,

$$D_0 = h/h_0, \tag{2}$$

$$F_r = \frac{\left(U_{\mathrm{cp}} - U_a\right)}{c_{\mathrm{gw}}} = \frac{\left(U_{\mathrm{cp}} - U_a\right)}{\sqrt{g\left(\frac{\Delta\theta_{\mathrm{vw}}}{\theta_{\mathrm{vw}}}\right)h_0}}, \tag{3}$$

where D_0 denotes the non-dimensional height determined by the ratio of h to h_0, where h is set equal to the height above the gravity current, where θ_e is greater than the surface θ_e of the ambient air, that is, the depth of gravity current. The term h_0 indicates the depth of the inversion layer, which is the level at which $\frac{d\theta}{dz}$ first drops below 0.005 Km^{-1}, $U_{\mathrm{cp}} - U_a$ represents the relative velocity between a cold pool and ambient air, c_{gw} the velocity of gravity wave, θ_{vw} the virtual potential temperature near surface, and $\Delta\theta_{\mathrm{vw}}$ the difference in θ_{vw} from the top to the bottom (surface) of the stable boundary layer.

To the SW, the disturbance formation at 2100–2200 LST was analyzed (Figure 14). The results indicate that $\boldsymbol{h}$ ranges from 1,200 m to 1,500 m, $\boldsymbol{h}_0$ ranges from 500 to 600 m, $\boldsymbol{D}_0$ is from 2.4 to 2.5, and $\boldsymbol{F}_r$ is from 1.56 to 1.6,

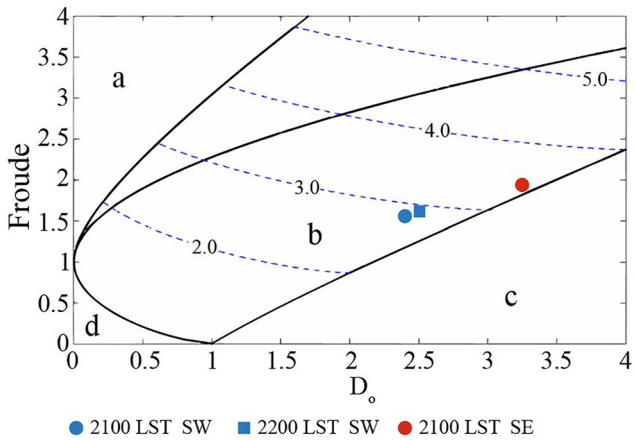

Figure 14. The non-dimensional parameters D_0 and F_r during the evolution of the bore. The two parameter spaces represent the predicted (a) supercritical, (b) partially blocked, (c) completely blocked and (d) subcritical flow regimes. The estimates of where the environment in the simulations appear in this phase space are also shown.

placing the disturbance in the region of a partial blocking regime of bore with a strength around 3 where type B undular bores usually form. The formation of type B undular bores in this regime are also consistent with the experiments using the related atmospheric measurements in Figure 9 of Rottman and Simpson (1989). Furthermore, the results are consistent with the development of the bore in Figures 11a–11d., that is, the bore is generated by the intrusion of cold pool (Figure 11a) and mixing enhanced as the cold pool becomes stronger (Figure 11b).

In the portion of the MCS to the SE, the undular bores were generated at the leading edge of the MCS as cold downdrafts reach the NSL (Figures 11e–11j). The analysis results at 2000 LST (Figure 11e) suggest that when the cooling downdrafts were evident, h is about 2,600 m, h_0 about 800 m, D_0 about 3.25, and F_r about 1.92. These values place the flow in the regime near the interface of partially blocked and complete blocking which allows an undular bore to be generated by the intrusion of cold air, that is, a current that moves along the top layer of the NSL (see Figure 11 in Rottman & Simpson, 1989).

5.2. Evolution of the Strong Mesoscale Downdraft Into the Atmospheric Environment

Previous studies also suggested that, as distinguished from their laboratory counterparts, atmospheric density currents (often called gravity currents in dynamical studies) are easily influenced by stratification, vertical shear, latent heating, and evaporative cooling (e.g., Haertel et al., 2001). Analysis in this section will follow previous studies to better understand the mechanisms of the bore generation in the SE portion of the MCS.

For example, according to Liu and Moncrieff (2000), stratification has a significant impact on the structure of the gravity current. As the Brunt–Väisälä frequency N increases from $\mathbf{0.004\ s^{-1}}$ to $\mathbf{0.016\ s^{-1}}$, the structure of the gravity current changes from a shallow body with a raised head to a body with multiple heads with leading heads dissipating periodically and new heads forming, suggesting the formation of bore-like disturbances. To the SE of the simulated MCS, the averaged N is estimated to be 0.027 $\mathbf{s^{-1}}$ producing an unsteady gravity current with bore generation according to Liu and Moncrieff (2000) with the strongest updrafts associated with bores at the leading edge.

Another relevant study by Haase and Smith (1989) also noted that the quantity μ can be used to illustrate how the stability and wind in the surrounding environment, as well as the characteristics of the cold pool influence the nature and evolution of an invasive gravity current. The term μ indicates a measure of the strength of the stable layer compared relative to the inflow strength and can be expressed as $\mu = c_0/c_{gr}$, where c_0 ($c_0 = \mathbf{2NH/\pi}$) denotes the phase speed of long waves of infinitesimal amplitude propagating in the stable layer, and H the vertical depth of the stable layer, and $c_{gr} = c_{gw}(\mathbf{0.88}F_r + \mathbf{0.45})$, which is the propagation speed of the gravity current in the absence of the stable layer.

According to Haase and Smith (1989), when $\mu \leq 0.7$, the gravity-current head separates from the feeder flow of cold air supplying it as c_0 increases, but it moves with the gravity current as a large-amplitude solitary-wave-like disturbance. At a large Froude number (F_r of ~1.13), two or more such waves may form, and the gravity current displays an undular bore. Following this notation, we calculated μ for the SE portion at 2000 LST, where c_0 is about 13.75 m s^{-1}, c_{gr} about 31.44 m s^{-1}, μ about 0.42 and F_r about 1.92. These values of μ and F_r also mean that the undular bore would evolve from the downdraft. Also, this phenomenon can be seen in the separating head of the gravity-current in Figure 11e and weaker feeder flow with undular waves in Figure 11i.

5.3. Maintenance of the Atmospheric Bore

The maintenance of the atmospheric bore is crucial for its ability to initiate or maintain nocturnal MCSs, in which the key point is that the vertical propagation of wave energy is prevented so that the waves can propagate horizontally. Crook (1988) suggested that scorer parameter l^2 can be used to explore the trapping mechanism of wave energy. The results indicated that energy was trapped through the internal reflection (Scorer, 1949) when

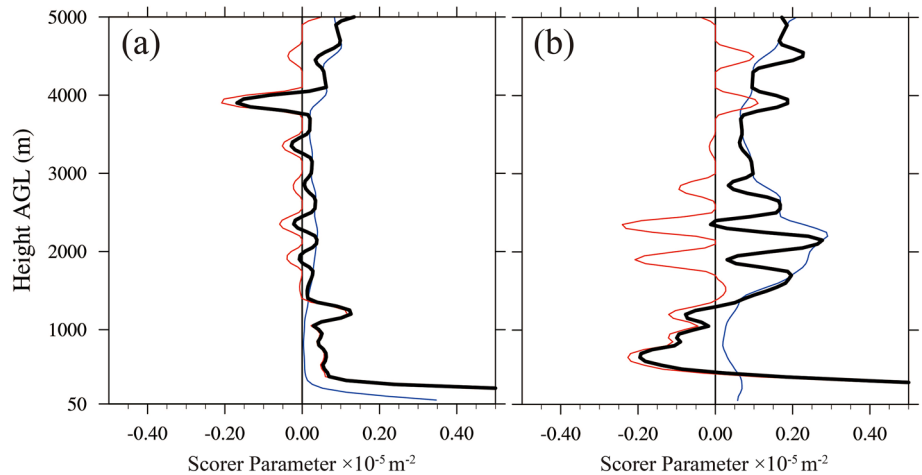

Figure 15. Variations of the Scorer parameter (thick black lines), static stability (blue lines) and curvature term (red lines) with height at 2200 LST in (a) the southwestern and (b) southeastern portions for the cross-section in Figures 11b and 11i.

Scorer parameter decreased from a positive to a negative value with height, due to the presence of critical layer or through the "curvature term." Details can be referred in Crook (1988).

In this approach, l^2 is given by (Equation 4).

$$l^2 = \frac{N^2}{(U - C_b)^2} - \frac{\partial^2 U / \partial z^2}{U - C_b}, \tag{4}$$

where the first term represents the static stability, U the wind speed in the direction of the bore motion, and C_b the wave speed. The second term includes the effects of the so-called "curvature" of the vertical profile of the horizontal wind. Note that, a higher static stability near the surface and a low-level jet in the opposite direction of the bore motion (which is more important), would both tend to result in larger values of l^2 near the surface, and thereby contribute to trapping wave energy (Haghi & Durran, 2021).

Recent studies (e.g., Haghi & Durran, 2021; Haghi et al., 2017) also suggest the trapping of wave energy often appears more through the curvature term in the Scorer parameter associated with the NLLJ. The importance of a strong low-level jet for maintaining the bore is further emphasized (Haghi & Durran, 2021). The first systematic study of bores in China also confirmed an obvious connection between the duration of the bores and the strong vertical wind shear that opposes the propagation of the bores associated with the NLLJ (Zhang et al., 2022).

The Scorer parameter was calculated at 2200 LST when the bore was initially generated in the SW and SE to determine if and how an appropriate wave duct is available. Both the SW and SE orientations showed a layer of positive Scorer parameter in the lowest one km with the Scorer parameter dropping sharply below 0.5 km (Figure 15). The phenomenon is related to relatively small fluctuations in the wind-profile curvature (Martin & Johnson, 2008). Layers of negative Scorer parameter were centered at 4 and 0.8 km (Figure 15), respectively, revealing a more favorable condition for bore propagation to the SE, though MCS failed to sustain convection due to the weaker CAPE and stronger CIN in this direction. The variation of the curvature term (red line) with height suggests that the layer of negative Scorer parameter in the SE (Figure 15b) may be due to a low-level jet with strong vertical shear opposing the propagation of the bore.

6. Summary and Implications

This investigation uses radar and surface observations and high-resolution numerical simulation using the WRF model to study the dynamics of atmospheric bores and their impact on the parent MCS in the non-uniform baroclinic environment over SNCP which is dominated by an early morning peak of precipitation during Mei-yu season (Xue et al., 2018). Previous investigations by Blake et al. (2017) and Chasteen et al. (2019) have shown that mesoscale variations over the Great Plains environment ahead of the MCS including spatial variations in the NLLJ impact the structure of bores and thus modify the structure of the MCS. The nocturnal environment during

warm season over the SNCP is usually highly non-uniform with a dominant Mei-yu front with a meridional gradient of equivalent potential temperature (θ_e) at the 850-hPa layer greater than 0.04 K km^{-1}. The structure and nature of the environment with the Mei-yu can vary in different periods and regions (Wang et al., 2022) due to a predominantly SE wind associated with the Pacific subtropical high and sometimes the presence of a sea breeze circulation near the coast (Huang et al., 2016). This pattern of E-SE winds leaves an area of cooler air in the lower layers along the coast, while inland the lower levels are become warmer due to the remnants of daytime solar radiation.

The onshore circulation and the NLLJ associated with the Mei-yu front create a different low level flow pattern. Thus, MCSs commonly experience a "nonlinear evolution" (e.g., sudden intensification or weakness; sudden structure change) over coastal region. The typical non-linear evolution is explored in this study with a focus on MCSs with accompanying bores. The presence of the nocturnal flow being influenced by the remnants of the sea breeze circulation makes these results relevant for other coastal regions. The ability to predict convection and high impact weather along coastal regions is a critical problem for society given the growing tendency for populations to concentrate along coast areas (e.g., Brunet et al., 2023).

Our study found that the structure of the MCS is greatly influenced by bores, the structure of which is modified by this mesoscale varying environment. To the SW, where the cold pool intrudes into the NSL resulting in the MCS transitioning from a southward propagating bow echo to a SW moving organized MCS associated with discrete propagation. In this environment with large/little CAPE/CIN to the SW, the bore lifts the air in front of the MCS to initiate convection or provide a more favorable environment for deep convection to subsequently be generated due to lifting by the cold pool. These processes maintain the MCS resulting in discrete propagation.

To the SE of the MCS in the coastal region, an undular bore was clearly generated by the MCS. However, the bore in this region failed to initiate new convection due to unfavorable, low/large CAPE/CIN environmental conditions resulting from the sea breeze. The bore in this region, however, provides an example of how an intrusion of a mesoscale downdraft extending into the NSL generate bores. A similar phenomenon appeared in our earlier case study of a bore over China (Zhang, Parsons, Xu, et al., 2020), which illustrates the evolution of the head of a cold pool separating from the cold pool and transiting to an undular bore. This phenomenon also can be found in the idealized simulation of a back-building MCS (Hitchcock & Schumacher, 2020), but at lower levels. It should be noted that this generation mechanism of a mesoscale downdraft interacting with the NSL is different than the commonly observed process of bores forming from the ambient flow interacting with the MCS's cold pool.

As noted in Grasmick et al. (2018), the outflow boundaries of an MCS may have different attributes, patterns, and feedback from the parent MCS due to the different upstream environments. This work provides a direct comparison of the variable responses of outflows under different ambient conditions. Moreover, distinct mechanisms of bore genesis over the SNCP are proposed. As indicated by the results of a systematic study in the SNCP (Zhang et al., 2022), the MCSs associated with bores typically have a well-organized leading front, perhaps implying that most of the bores over SNCP are generated from strong downdrafts. It is not surprising that in the moist environment during the monsoon season, the convective cold pool is weak and does not have enough negative buoyancy to intrude into the NSL. Thus, the strong downdrafts reaching the surface, perhaps driven by water loading in this moist environment may play a more critical role in generating bores in this region. Figuratively speaking, undular bores over the Southern Great Plains (Haghi et al., 2017) can be compared to the ripples on the surface of a shallow pool when a frog swims below, while these bores over the SNCP can be compared to the ripples when a frog jumps into a pool. This finding requires confirmation from a study of a larger number of MCSs with bores, especially, observed and confirmed by vertical profiling instruments.

This study also reveals how the cold pool-bore interaction depends on variations in the nocturnal environment so that the stability and vertical shear associated with low-level jets in the nocturnal environment are essential factors in determining whether and how a bore is generated and evolves. The findings of an elevated bore in the Zhang, Parsons, and Wang (2020) study over the Great Plains also suggests these essential factors extend to heights well above the NSL. The strength of the cold pool also matters so that both an accurate representation of microphysics and kinematics of the MCS (e.g., Bodine & Rasmussen, 2017) and the character of the ambient environment are likely to improve the forecast accuracy of the bores and MCS over the SNCP. This study also illustrates the challenges of accurately representing nocturnal convection in weather and climate models with parameterized convection as the interaction between cold pools, bores and the NSL, and mesoscale variations in the environment can determine the evolution, movement, and structure of nocturnal MCS.

Data Availability Statement

The ERA5 reanalysis data can be freely downloaded (available at https://cds.climate.copernicus.eu/cdsapp#!/dataset/reanalysis-era5-pressure-levels). Due to policies for observational data to the public, only two files of radar observation for Figure 2 are uploaded to repository for archive (Zhang, 2023).

Acknowledgments
This work was funded by National Natural Science Foundation of China (42122036), Open Project of the High Impact Weather Key Laboratory of CMA, National Natural Science Foundation of China (42105007, 42005009), The Open Grants of the State Key Laboratory of Severe Weather (2022LASW-B01), the Basic Research Fund of CAMS (2021Y016, 2021Z003), and the Jiangsu Innovative and Enterpreneurial Talent Programme (JSSCBS20211317). The simulations were performed on the supercomputer at the School of Atmospheric Science, Nanjing University. The participation of one of the researchers (David B. Parsons) is supported by NSF Grant AGS-1921587, which aims to increase our understanding of bores and nocturnal MCSs. We are grateful for our discussions with Peter Bechtold (ECMWF) and Alan Shapiro (OU) on the challenges of parameterizing nocturnal MCSs and bore dynamics.

References

Adams-Selin, R. D., & Johnson, R. H. (2013). Examination of gravity waves associated with the 13 March 2003 bow echo. *Monthly Weather Review*, *141*(11), 3735–3756. https://doi.org/10.1175/MWR-D-12-00343.1

Baines, P. G. (1984). A unified description of two-layer flow over topography. *Journal of Fluid Mechanics*, *146*, 127–167. https://doi.org/10.1017/S0022112084001798

Baines, P. G., & Davies, P. A. (1980). Laboratory studies of topographic effects in rotating and/or stratified fluids (N80-33811 24-42). In *WMO orographic effects in planetary flows* (pp. 233–299). WMO.

Bechtold, P., Semane, N., Lopez, P., Chaboureau, J. P., Beljaars, A., & Bormann, N. (2014). Representing equilibrium and nonequilibrium convection in large-scale models. *Journal of the Atmospheric Sciences*, *71*(2), 734–753. https://doi.org/10.1175/JAS-D-13-0163.1

Becker, T., Bechtold, P., & Sandu, I. (2021). Characteristics of convective precipitation over tropical Africa in storm-resolving global simulations. *Quarterly Journal of the Royal Meteorological Society*, *147*(741), 4388–4407. https://doi.org/10.1002/qj.4185

Birch, C. E., & Reeder, M. J. (2013). Wave-cloud lines over northwest Australia. *Quarterly Journal of the Royal Meteorological Society*, *139*(674), 1311–1326. https://doi.org/10.1002/qj.2043

Blake, B. T., Parsons, D. B., Haghi, K. R., & Castleberry, S. G. (2017). The structure, evolution, and dynamics of a nocturnal convective system simulated using the WRF-ARW Model. *Monthly Weather Review*, *145*(8), 3179–3201. https://doi.org/10.1175/MWR-D-16-0360.1

Bodine, D. J., & Rasmussen, K. L. (2017). Evolution of mesoscale convective system organizational structure and convective line propagation. *Monthly Weather Review*, *145*(9), 3419–3440. https://doi.org/10.1175/MWR-D-16-0406.1

Brunet, G., Parsons, D. B., Ivanov, D., Lee, B., Bauer, P., Bernier, N. B., et al. (2023). Advancing weather and climate forecasting for our changing world. *Bulletin of the American Meteorological Society*, *104*(4), E909–E927. https://doi.org/10.1175/BAMS-D-21-0262.1

Bryan, G. H., & Rotunno, R. (2014). The optimal state for gravity currents in shear. *Journal of the Atmospheric Sciences*, *71*(1), 448–468. https://doi.org/10.1175/JAS-D-13-0156.1

Carbone, R. E., & Tuttle, J. D. (2008). Rainfall occurrence in the U.S. warm season: The diurnal cycle. *Journal of Climate*, *21*(16), 4132–4146. https://doi.org/10.1175/2008JCLI2275.1

Carbone, R. E., Tuttle, J. D., Ahijevych, D. A., & Trier, S. B. (2002). Inferences of predictability associated with warm season precipitation episodes. *Journal of the Atmospheric Sciences*, *59*(13), 2033–2056. https://doi.org/10.1175/1520-0469(2002)059<2033:IOPAWW>2.0.CO;2

Chasteen, M. B., Koch, S. E., & Parsons, D. B. (2019). Multi-scale processes enabling the longevity and daytime persistence of a nocturnal mesoscale convective system. *Monthly Weather Review*, *147*(2), 733–761. https://doi.org/10.1175/MWR-D-18-0233.1

Clark, A. J. (2017). Generation of ensemble mean precipitation forecasts from convection-allowing ensembles. *Weather and Forecasting*, *32*(4), 1569–1583. https://doi.org/10.1175/WAF-D-16-0199.1

Collins, W. D., Rasch, P. J., Boville, B. A., McCaa, J., Williamson, D. L., Kiehl, J. T., et al. (2004). Description of the NCAR community atmosphere model (CAM 3.0). NCAR tech. Note NCAR/TN-4641STR (p. 214). https://doi.org/10.5065/D63N21CH

Coniglio, M. C., Corfidi, S. F., & Kain, J. S. (2012). Views on applying RKW theory: An illustration using the 8 May 2009 derecho-producing convective system. *Monthly Weather Review*, *140*(3), 1023–1043. https://doi.org/10.1175/MWR-D-11-00026.1

Corfidi, S. F., Corfidi, S. J., & Schultz, D. M. (2008). Elevated convection and castellanus: Ambiguities, significance, and questions. *Weather and Forecasting*, *23*(6), 1280–1303. https://doi.org/10.1175/2008WAF2222118.1

Cotton, W. R., George, R. L., Wetzel, P. J., & McAnelly, R. L. (1983). A long-lived mesoscale convective complex. Part I: The mountain–generated component. *Monthly Weather Review*, *111*(10), 1893–1918. https://doi.org/10.1175/1520-0493(1983)111<1893:ALLMCC>2.0.CO;2

Crook, N. A. (1988). Trapping of low-level internal gravity waves. *Journal of the Atmospheric Sciences*, *45*(10), 1533–1541. https://doi.org/10.1175/1520-0469(1988)045<1533:TOLLIG>2.0.CO;2

Davies, L., Reeder, M. J., & Lane, T. P. (2017). A climatology of atmospheric pressure jumps over southeastern Australia. *Quarterly Journal of the Royal Meteorological Society*, *143*(702), 439–449. https://doi.org/10.1002/qj.2933

Davis, C. A., & Galarneau, T. J. (2009). The vertical structure of mesoscale convective vortices. *Journal of the Atmospheric Sciences*, *66*(3), 686–704. https://doi.org/10.1175/2008JAS2819.1

Duda, J. D., Wang, X., Kong, F., & Xue, M. (2014). Using varied microphysics to account for uncertainty in warm-season QPF in a convection-allowing ensemble. *Monthly Weather Review*, *142*(6), 2198–2219. https://doi.org/10.1175/MWR-D-13-00297.1

Fovell, R. G., Mullendore, G. L., & Kim, S. H. (2006). Discrete propagation in numerically simulated nocturnal squall lines. *Monthly Weather Review*, *134*(12), 3735–3752. https://doi.org/10.1175/MWR3268.1

French, A. J., & Parker, M. D. (2010). The response of simulated nocturnal convective systems to a developing low-level jet. *Journal of the Atmospheric Sciences*, *67*(10), 3384–3408. https://doi.org/10.1175/2010JAS3329.1

Fritsch, J. M., & Carbone, R. E. (2004). Improving quantitative precipitation forecasts in the warm season: A USWRP research and development strategy. *Bulletin of the American Meteorological Society*, *85*(7), 955–966. https://doi.org/10.1175/BAMS-85-7-955

Grasmick, C., Geerts, B., Turner, D. D., Wang, Z., & Weckwerth, T. M. (2018). The relation between nocturnal MCS evolution and its outflow boundaries in the stable boundary layer: An observational study of the 15 July 2015 MCS in PECAN. *Monthly Weather Review*, *146*(10), 3203–3226. https://doi.org/10.1175/MWR-D-18-0169.1

Geerts, B., Parsons, D., Ziegler, C. L., Weckwerth, T. M., Biggerstaff, M. I., Clark, R. D., et al. (2017). The 2015 plains elevated convection at night field project. *Bulletin of the American Meteorological Society*, *98*(4), 767–786. https://doi.org/10.1175/bams-d-15-00257.1

Guan, P., Chen, G., Zeng, W., & Liu, Q. (2020). Corridors of Mei-Yu-season rainfall over eastern China. *Journal of Climate*, *33*(7), 2603–2626. https://doi.org/10.1175/JCLI-D-19-0649.1

Haase, S. P., & Smith, R. K. (1989). The numerical simulation of atmospheric gravity currents. Part II. Environments with stable layers. *Geophysical & Astrophysical Fluid Dynamics*, *46*(1–2), 35–51. https://doi.org/10.1080/03091928908208903

Haertel, P. T., Johnson, R. H., & Tulich, S. N. (2001). Some simple simulations of thunderstorm outflows. *Journal of the Atmospheric Sciences*, *58*(5), 504–516. https://doi.org/10.1175/1520-0469(2001)058<0504:SSSOTO>2.0.CO;2

Haghi, K. R., & Durran, D. R. (2021). On the dynamics of atmospheric bores. *Journal of the Atmospheric Sciences*, *78*(1), 313–327. https://doi.org/10.1175/BAMS-D-17-0250.1

Haghi, K. R., Geerts, B., Chipilski, H. G., Johnson, A., Degelia, S., Imy, D., et al. (2019). Bore-ing into nocturnal convection. *Bulletin of the American Meteorological Society*, *100*(6), 1103–1121. https://doi.org/10.1175/BAMS-D-17-0250.1

Haghi, K. R., Parsons, D. B., & Shapiro, A. (2017). Bores observed during IHOP_2002: The relationship of bores to the nocturnal environment. *Monthly Weather Review*, *145*(10), 3929–3946. https://doi.org/10.1175/MWR-D-16-0415.1

Hersbach, H., Bell, B., Berrisford, P., Biavati, G., Horányi, A., Muñoz Sabater, J., et al. (2018). ERA5 hourly data on pressure levels from 1979 to present [Dataset]. Copernicus Climate Change Service (C3S) Climate Data Store (CDS), *10*. https://doi.org/10.24381/cds.bd0915c6

Hitchcock, S. M., & Schumacher, R. S. (2020). Analysis of back-building convection in simulations with a strong low-level stable layer. *Monthly Weather Review*, *148*(9), 3773–3797. https://doi.org/10.1175/MWR-D-19-0246.1

Houghton, D. D., & Kasahara, A. (1968). Nonlinear shallow fluid flow over an isolated ridge. *Communications on Pure and Applied Mathematics*, *21*(1), 1–23. https://doi.org/10.1002/cpa.3160210103

Houze, R. A., Jr. (2018). 100 years of research on mesoscale convective systems. *Meteorological Monographs*, *59*, 17–21. https://doi.org/10.1175/AMSMONOGRAPHS-D-18-0001.1

Huang, M., Gao, Z., Miao, S., & Xu, X. (2016). Characteristics of sea breezes over the Jiangsu coastal area, China. *International Journal of Climatology*, *36*(12), 3908–3916. https://doi.org/10.1002/joc.4602

Kain, J. S. (2004). The Kain–Fritsch convective parameterization: An update. *Journal of Applied Meteorology and Climatology*, *43*(1), 170–181. https://doi.org/10.1175/1520-0450(2004)043,0170:TKCPAU.2.0.CO;2

Keenan, T. D., & Carbone, R. E. (2008). Propagation and diurnal evolution of warm season cloudiness in the Australian and Maritime Continent region. *Monthly Weather Review*, *136*(3), 973–994. https://doi.org/10.1175/2007MWR2152.1

Knupp, K. (2006). Observational analysis of a gust front to bore to solitary wave transition within an evolving nocturnal boundary layer. *Journal of the Atmospheric Sciences*, *63*(8), 2016–2035. https://doi.org/10.1175/JAS3731.1

Koch, S. E., & Clark, W. L. (1999). A nonclassical cold front observed during COPS-91: Frontal structure and the process of severe storm initiation. *Journal of the Atmospheric Sciences*, *56*(16), 2862–2890. https://doi.org/10.1175/1520-0469(1999)056,2862:ANCFOD.2.0.CO;2

Koch, S. E., Feltz, W., Fabry, F., Pagowski, M., Geerts, B., Bedka, K. M., et al. (2008). Turbulent mixing processes in atmospheric bores and solitary waves deduced from profiling systems and numerical simulation. *Monthly Weather Review*, *136*(4), 1373–1400. https://doi.org/10.1175/2007MWR2252.1

Koch, S. E., Flamant, C., Wilson, J. W., Gentry, B. M., & Jamison, B. D. (2008). An atmospheric soliton observed with Doppler radar, differential absorption lidar, and a molecular Doppler lidar. *Journal of Atmospheric and Oceanic Technology*, *25*(8), 1267–1287. https://doi.org/10.1175/2007JTECHA951.1

Laing, A. G., & Fritsch, J. M. (1993). Mesoscale convective complexes in Africa. *Monthly Weather Review*, *121*(8), 2254–2263. https://doi.org/10.1175/1520-0493(1993)121<2254:MCCIA>2.0.CO;2

Liu, C., & Moncrieff, M. W. (2000). Simulated density currents in idealized stratified environments. *Monthly Weather Review*, *128*(5), 1420–1437. https://doi.org/10.1175/1520-0493(2000)128<1420:SDCIIS>2.0.CO;2

Liu, C., & Moncrieff, M. W. (2017). Shear-parallel mesoscale convective systems in a moist low-inhibition mei-yu front environment. *Journal of the Atmospheric Sciences*, *74*(12), 4213–4228. https://doi.org/10.1175/JAS-D-17-0121.1

Lombardo, K., & Kumjian, M. R. (2022). Observations of the discrete propagation of a mesoscale convective system during RELAMPAGO–CACTI. *Monthly Weather Review*, *150*(8), 2111–2138. https://doi.org/10.1175/MWR-D-21-0265.1

Long, R. R. (1954). Some aspects of the flow of stratified fluids: II. Experiments with a two-fluid system. *Tellus*, *6*(2), 97–115. https://doi.org/10.1111/j.2153-3490.1954.tb01100.x

Loveless, D. M., Wagner, T. J., Turner, D. D., Ackerman, S. A., & Feltz, W. F. (2019). A composite perspective on bore passages during the PECAN campaign. *Monthly Weather Review*, *147*(4), 1395–1413. https://doi.org/10.1175/MWR-D-18-0291.1

Maddox, R. A., Canova, F., & Hoxit, L. R. (1980). Meteorological characteristics of flash flood events over the western United States. *Monthly Weather Review*, *108*(11), 1866–1877. https://doi.org/10.1175/1520-0493(1980)108<1866:MCOFFE>2.0.CO;2

Martin, E. R., & Johnson, R. H. (2008). An observational and modeling study of an atmospheric internal bore during NAME 2004. *Monthly Weather Review*, *136*(11), 4150–4167. https://doi.org/10.1175/2008MWR2486.1

Meng, Z., Yan, D., & Zhang, Y. (2013). General features of squall lines in East China. *Monthly Weather Review*, *141*(5), 1629–1647. https://doi.org/10.1175/MWR-D-12-00208.1

Meng, Z., & Zhang, Y. (2012). On the squall lines preceding landfalling tropical cyclones in China. *Monthly Weather Review*, *140*(2), 445–470. https://doi.org/10.1175/MWR-D-10-05080.1

Min, C., Chen, S., Gourley, J. J., Chen, H., Zhang, A., Huang, Y., & Huang, C. (2019). Coverage of China new generation weather radar network. *Advances in Meteorology*, *2019*, 1–10. https://doi.org/10.1155/2019/5789358

Morrison, H., Curry, C. J. A., & Khvorostyanov, V. I. (2005). A new double-moment microphysics parameterization for application in cloud and climate models. Part I: Description. *Journal of the Atmospheric Sciences*, *62*(6), 1665–1677. https://doi.org/10.1175/JAS3446.1

Morrison, H., & Milbrandt, J. A. (2015). Parameterization of cloud microphysics based on the prediction of bulk ice particle properties. Part I: Scheme description and idealized tests. *Journal of the Atmospheric Sciences*, *72*(1), 287–311. https://doi.org/10.1175/JAS-D-14-0065.1

Morrison, H., Thompson, G., & Tatarskii, V. (2009). Impact of cloud microphysics on the development of trailing stratiform precipitation in a simulated squall line: Comparison of one and two-moment schemes. *Monthly Weather Review*, *137*(3), 991–1007. https://doi.org/10.1175/2008MWR2556.1

Osborne, S. R., & Lapworth, A. (2017). Initiation and propagation of an atmospheric bore in a numerical forecast model: A comparison with observations. *Journal of Applied Meteorology and Climatology*, *56*(11), 2999–3016. https://doi.org/10.1175/JAMC-D-17-0045.1

Parker, M. D. (2021). Self-organization and maintenance of simulated nocturnal convective systems from PECAN. *Monthly Weather Review*, *149*(4), 999–1022. https://doi.org/10.1175/MWR-D-20-0263.1

Parker, M. D., & Ahijevych, D. A. (2007). Convective episodes in the east-central United States. *Monthly Weather Review*, *135*(11), 3707–3727. https://doi.org/10.1175/2007MWR2098.1

Parker, M. D., & Johnson, R. H. (2000). Organizational modes of midlatitude mesoscale convective systems. *Monthly Weather Review*, *128*(10), 3413–3436. https://doi.org/10.1175/1520-0493(2001)129<3413:OMOMMC>2.0.CO;2

Parsons, D. B. (1992). An explanation of intense frontal updrafts and narrow cold-frontal rainbands. *Journal of the Atmospheric Sciences*, *49*(19), 1810–1825. https://doi.org/10.1175/1520-0469(1992)049<1810:AEFIFU>2.0.CO;2

Parsons, D. B., Haghi, K. R., Halbert, K. T., Elmer, B., & Wang, J. (2019). The potential role of atmospheric bores and gravity waves in the initiation and maintenance of nocturnal convection over the Southern Great Plains. *Journal of the Atmospheric Sciences*, *76*(1), 43–68. https://doi.org/10.1175/JAS-D-17-0172.1

Peters, J. M., Nielsen, E. R., Parker, M. D., Hitchcock, S. M., & Schumacher, R. S. (2017). The impact of low-level moisture errors on model forecasts of an MCS observed during PECAN. *Monthly Weather Review*, *145*(9), 3599–3624. https://doi.org/10.1175/MWR-D-16-0296.1

Pleim, J. E. (2006). A simple, efficient solution of flux–profile relationships in the atmospheric surface layer. *Journal of Applied Meteorology and Climatology*, *45*(2), 341–347. https://doi.org/10.1175/JAM2339.1

Pleim, J. E. (2007). A combined local and nonlocal closure model for the atmospheric boundary layer. Part I: Model description and testing. *Journal of Applied Meteorology and Climatology*, *46*(9), 1383–1395. https://doi.org/10.1175/JAM2539.1

Reif, D. W., & Bluestein, H. B. (2017). A 20-year climatology of nocturnal convection initiation over the central and southern Great Plains during the warm season. *Monthly Weather Review*, *145*(5), 1615–1639. https://doi.org/10.1175/MWR-D-16-0340.1

Rottman, J. W., & Simpson, J. E. (1989). The formation of internal bores in the atmosphere: A laboratory model. *Quarterly Journal of the Royal Meteorological Society*, *115*(488), 941–963. https://doi.org/10.1002/qj.49711548809

Rotunno, R., Klemp, J. B., & Weisman, M. L. (1988). A theory for strong, long-lived squall lines. *Journal of the Atmospheric Sciences*, *45*(3), 463–485. https://doi.org/10.1175/1520-0469(1988)045<0463:ATFSLL>2.0.CO;2

Scorer, R. S. (1949). Theory of waves in the lee of mountains. *Quarterly Journal of the Royal Meteorological Society*, *75*(323), 41–56. https://doi.org/10.1002/qj.49707532308

Skamarock, W. C., Klemp, J. B., Dudhia, J., Gill, D. O., Barker, D. M., Wang, W., & Powers, J. G. (2008). A description of the advanced research WRF version 3. NCAR technical note-475+ STR. https://doi.org/10.5065/D68S4MVH

Stensrud, D. J., Bao, J. W., & Warner, T. T. (2000). Using initial condition and model physics perturbations in short-range ensemble simulations of mesoscale convective systems. *Monthly Weather Review*, *128*(7), 2077–2107. https://doi.org/10.1175/1520-0493.(2000)128,2077:UICAMP.2.0.CO;2

Stensrud, D. J., Coniglio, M. C., Davies-Jones, R. P., & Evans, J. S. (2005). Comments on "A theory for long-lived squall lines revisited.". *Journal of the Atmospheric Sciences*, *62*(8), 2989–2996. https://doi.org/10.1175/JAS3514.1

Tang, S., Gleckler, P., Xie, S., Lee, J., Ahn, M. S., Covey, C., & Zhang, C. (2021). Evaluating the diurnal and semidiurnal cycle of precipitation in CMIP6 models using satellite-and ground-based observations. *Journal of Climate*, *34*(8), 3189–3210. https://doi.org/10.1175/JCLI-D-20-0639.1

Wang, X., Zhou, R., Deng, Y., Cui, C., Hu, Y., Wang, J., & Liu, H. (2022). Symbiotic relationship between Mei-Yu rainfall and the morphology of Mei-Yu front. *Journal of Hydrometeorology*, *23*(1), 87–100. https://doi.org/10.1175/JHM-D-21-0068.1

Watson, C. D., & Lane, T. P. (2016). A case of an undular bore and prefrontal precipitation in the Australian Alps. *Monthly Weather Review*, *144*(7), 2623–2644. https://doi.org/10.1175/MWR-D-15-0355.1

Wetzel, P. J., Cotton, W. R., & McAnelly, R. L. (1983). A long-lived mesoscale convective complex. Part II: Evolution and structure of the mature complex. *Monthly Weather Review*, *111*(10), 1919–1937. https://doi.org/10.1175/1520-0493(1983)111<1919:ALLMCC>2.0.CO;2

Xue, M., Luo, X., Zhu, K., Sun, Z., & Fei, J. (2018). The controlling role of boundary layer inertial oscillations in Meiyu frontal precipitation and its diurnal cycles over China. *Journal of Geophysical Research: Atmospheres*, *123*(10), 5090–5115. https://doi.org/10.1029/2018JD028368

Yang, X., Fei, J., Huang, X., Cheng, X., Carvalho, L. M., & He, H. (2015). Characteristics of mesoscale convective systems over China and its vicinity using geostationary satellite FY2. *Journal of Climate*, *28*(12), 4890–4907. https://doi.org/10.1175/JCLI-D-14-00491.1

Young, G. S., Perugini, S. M., & Fairall, C. W. (1995). Convective wakes in the equatorial western Pacific during TOGA. *Monthly Weather Review*, *123*(1), 110–123. https://doi.org/10.1175/1520-0493(1995)123<0110:CWITEW>2.0.CO;2

Yu, R., Xu, Y., Zhou, T., & Li, J. (2007). Relation between rainfall duration and diurnal variation in the warm season precipitation over central eastern China. *Geophysical Research Letters*, *34*(13), L13703. https://doi.org/10.1029/2007GL030315

Zhang, S. (2023). Data for: The development of atmospheric bores in non-uniform baroclinic environments and their roles in the maintenance, structure, and evolution of an MCS submitted to JGR atmospheric [Dataset]. Figshare.v2. https://doi.org/10.6084/m9.figshare.22338223

Zhang, S., Parsons, D. B., & Wang, Y. (2020). Wave disturbances and their role in the maintenance, structure, and evolution of a mesoscale convection system. *Journal of the Atmospheric Sciences*, *77*(1), 51–77. https://doi.org/10.1175/JAS-D-18-0348.1

Zhang, S., Parsons, D. B., Xu, X., Sun, J., Wu, T., Xu, F., et al. (2022). Bores observed during the warm season of 2015–2019 over the southern North China Plain. *Geophysical Research Letters*, *49*(15), e2022GL099205. https://doi.org/10.1029/2022GL099205

Zhang, S., Parsons, D. B., Xu, X., Wang, Y., Liu, J., Abulikemu, A., et al. (2020). A modeling study of an atmospheric bore associated with a nocturnal convective system over China. *Journal of Geophysical Research: Atmospheres*, *125*(18), e2019JD032279. https://doi.org/10.1029/2019JD032279